Journal of Power Sources 592 (2024) 233893

Contents lists available at ScienceDirect

Journal of Power Sources

journal homepage: www.elsevier.com/locate/jpowsour

# Long-term stability of lithium–sulfur batteries via synergistic integration of nitrogen-doped graphitic carbon-coated cobalt selenide nanocrystals within porous three-dimensional graphene-carbon nanotube microspheres

Rakesh Saroha [a,1], Hye Seon Ka [a,1], Gi Dae Park [b], Chungyeon Cho [c], Dong-Won Kang [d,**], Jung Sang Cho [a,*]

[a] Department of Engineering Chemistry, Chungbuk National University, Chungbuk, 361-763, Republic of Korea
[b] Department of Advanced Materials Engineering, Chungbuk National University, Chungbuk, 361-763, Republic of Korea
[c] Department of Carbon Convergence Engineering, College of Engineering, Wonkwang University, Iksan, 54538, Republic of Korea
[d] School of Energy Systems Engineering, Chung-Ang University, 84, Heukseok-Ro, Dongjak-Gu, Seoul, 06974, Republic of Korea

## HIGHLIGHTS

- Porous microspheres with three-dimensional rGO–CNT framework is prepared.
- Comprising well-entangled N–doped graphitic carbon-coated $CoSe_2$ nanocrystals.
- $CoSe_2$ nanocrystals ensure efficient anchoring of lithium polysulfide.
- The rGO–CNT framework improves the structural integrity and overall conductivity.
- P–$CoSe_2$@NGC/rGO–CNT interlayer exhibits improved electrochemical performance.

## GRAPHICAL ABSTRACT

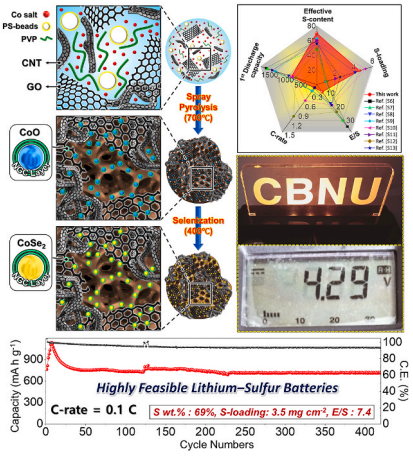


## ARTICLE INFO

*Keywords:*
Lithium-sulfur batteries
Spray pyrolysis
Multifunctional interlayers
Metal selenide
Graphene
Carbon nanotube

## ABSTRACT

Three-dimensional porous microspheres consist of highly conductive reduced graphene oxide-carbon nanotube (rGO–CNT) framework with well-embedded cobalt selenide ($CoSe_2$) nanocrystals coated with N-doped graphitic carbon (NGC) were synthesized (referred as "P–$CoSe_2$@NGC/rGO–CNT" microspheres) and utilized as an electrocatalytic interlayer to enhance the performance of lithium-sulfur (Li–S) batteries. The incorporation of the NGC layer and rGO–CNT framework not only enhances the electronic conductivity significantly but also offers numerous conductive pathways (primary and secondary) for efficient electron transport. Macropores ($\varphi$ = 100

* Corresponding author.
** Corresponding author.
*E-mail addresses:* kangdwn@cau.ac.kr (D.-W. Kang), jscho@cbnu.ac.kr (J.S. Cho).
[1] These authors contributed equally.

https://doi.org/10.1016/j.jpowsour.2023.233893
Received 13 August 2023; Received in revised form 8 November 2023; Accepted 23 November 2023

nm) formed by the decomposition of PS nanobeads ($\varphi = 200$ nm) guarantee effective electrolyte penetration and short diffusion pathways. Moreover, the $CoSe_2$ nanocrystals offer a multitude of polar active sites that effectively anchor polysulfide intermediates, reducing the loss of active material. Benefiting from the nanostructure merits, Li–S cells featuring a P–$CoSe_2$@NGC/rGO–CNT-coated separator and a conventional sulfur electrode demonstrated outstanding rate capability (up to 2.0 C) and remarkable cycling stability (1000 cycles at 2.0 C). Even under more demanding cell conditions, such as high sulfur content (71 %), high sulfur loading (4.6 mg $cm^{-2}$), and low E/S (5.6 μL $mg^{-1}$) ratio, the cell exhibits impressive cycling stability with 420 cycles at 0.1 C, along with feasible rate performance up to 0.3 C.

## 1. Introduction

Despite remarkable progress in the development of long-lasting and highly durable lithium-ion batteries (LIBs), several technical issues must be effectively addressed to expand their range of applications [1–6]. For instance, the current gravimetric or volumetric energy densities of LIBs are insufficient for applications such as power grids, unmanned aerial vehicles, and electric vehicles [7–11]. In this context, lithium-sulfur (Li–S) batteries have received tremendous attention from the research community as an emerging technology, primarily because of their high specific discharge capacity (1675 mA h $g^{-1}$) and impressive gravimetric (2600 Wh $kg^{-1}$) and volumetric (2800 Wh $L^{-1}$) energy density values [12–15]. Additionally, their low cost resulting from surplus raw materials (elemental sulfur, $S_8$), nominal discharge voltage *vs.* $Li/Li^+$ (~2.1 V), and non-hazardous nature make them particularly suitable for commercial applications [16–19]. Nevertheless, Li–S batteries are still facing considerable challenges that impede their practical application, primarily stemming from the fundamental weaknesses present in the redox process of $S_8$ [20–22]. For instance, during the initial reduction process, higher-order lithium polysulfide (h-PS) species formed from $S_8$ tend to diffuse towards the Li-metal anode because of concentration gradients and deposit as lower-order lithium polysulfide (l-PS), resulting in the formation of lithium sulfide ($Li_2S$) on the anode surface [23–26]. During oxidation, l-PS transforms back into h-PS and migrates back to the sulfur electrode under the influence of an electric field, resulting in the well-known shuttle effect [27–30]. This parasitic shuttle process leads to self-discharge processes, significant active material loss, and inferior cycling performance owing to unstable interfaces at cathode and anode [31–33]. Besides, the poor electronic conductivity of the charge and discharge products, along with the large volume variations between S and $Li_2S$, also contribute to critical battery issues such as electrode pulverization [34–36]. From a commercialization perspective, innovative strategies are required for advanced cathode host, anode protection, highly stable electrolytes, and even for advanced separators [37–40].

To address the above drawbacks, researchers have extensively investigated the use of various conductive and porous carbon hosts to confine elemental sulfur within a porous skeleton, which has been effective in reducing the shuttle effect to a certain extent [41]. However, the nonpolar nature of the carbon materials results in weak interactions with the polysulfide species, thus not fully suppress the shuttling effect in organic electrolytes [1]. Another promising strategy that has gained considerable interest is the incorporation of cathodic interlayers, which act as catalytic barriers for the physical or chemical adsorption of polysulfide species, thereby improving the electrochemical performance considerably [42]. The polar components in interlayer materials provide numerous active sites for the efficient anchoring of lithium polysulfides (LiPSs), effectively impeding the diffusion of h-PS towards the anode. Previous studies have explored various polar materials as cathodic interlayers, including conductive porous carbons [43], metal sulfides [44], metal oxides [17], metal nitrides [18], metal phosphides [33], metal catalyst [45], freestanding cathodes [46], and many more [47–52], to enhance the Li–S batteries performance. In particular, transition-metal selenides (TMSes) have garnered significant attention owing to their high surface polarity, narrow bandgap, and outstanding conductivity compared to the oxides or sulfides [1,7]. Furthermore, the presence of lithophilic and sulfiphilic sites in TMSes ensures the suppression of dendrite formation and efficient anchoring of polysulfide species, thereby improving the utilization of active materials. For instance, Chen et al., reported utilization of $CoSe_2$@C–N/CNT-modified separator to enhance the electrochemical performance of Li–S cell and reported a discharge capacity of 761 mA h $g^{-1}$ at the end of 300th cycle at 1.0 C-rate [53]. However, all the electrochemical tests were performed using S-CNT composite with a low active material loading of just 1.0 mg $cm^{-2}$.

In this study, we have developed three-dimensional (3D) porous microspheres comprising a highly conductive reduced graphene oxide and carbon nanotube (rGO–CNT) framework with well-embedded N-doped graphitic carbon (NGC)-coated $CoSe_2$ nanocrystals (P–$CoSe_2$@NGC/rGO–CNT microspheres) using a facile spray pyrolysis technique, followed by selenization. Spray pyrolysis, an aerosol-assisted method, has gained prominence due to its cost-effectiveness and continuous operation, making it commercially viable. This process involves atomizing precursor solution droplets with ultrasonic power, followed by their evaporation and decomposition in a thermal reactor, which takes only a few seconds to several tens of seconds. The as-prepared microspheres were utilized as catalytic barriers to enhance the performance of Li–S batteries. The NGC layer and rGO–CNT framework significantly enhanced the total electronic conductivity of the nanostructures. In particular, the NGC layer serves as the primary pathway for facilitating fast and continuous electron transfer, whereas the self-supporting rGO–CNT framework behaves as secondary pathways for subsequent electron transfer during the electrochemical process. Additionally, the presence of rGO-CNT stabilizes the 3D porous matrix by effectively bridging the rGO nanosheets with the CNTs and protecting them from detachment. To introduce porosity into the 3D conductive matrix, we used a suspension of polystyrene (PS) nanobeads ($\varphi = 200$ nm) as a porogen. The resulting porous structure allows smooth diffusion of charged species by shortening the effective charge diffusion length. Moreover, it reduces the electrolyte volume consumption and helps mitigate the severe volume variations that occur during the lithiation/delithiation processes. Accordingly, the Li–S cells featuring the P–$CoSe_2$@NGC/rGO–CNT catalytic interlayer and regular S electrode (~2 mg $cm^{-2}$) exhibited satisfactory rate capability (up to 2.0 C) and demonstrated excellent cycling performance (1000 cycles at 2.0 C). Even under extreme battery conditions (effective S–content = 71 %, S-loading = 4.6 mg $cm^{-2}$, and E/S = 5.6 μL $mg^{-1}$), the Li–S cells displayed excellent cycling stability (420 cycles at 0.1 C). The synthesis technique presented in this study offers new insights into the controlled synthesis of sophisticated nanostructures, thereby enabling the development of highly durable and long-lasting Li–S batteries.

## 2. Experimental

### 2.1. Synthesis process

Three-dimensional porous microspheres comprising highly conductive reduced graphene oxide–carbon nanotube (rGO–CNT) framework and well-implanted N-doped graphitic carbon-coated $CoSe_2$ nanocrystals (denoted as "P–$CoSe_2$@NGC/rGO–CNT" microspheres) were synthesized. The synthesis process involved spray pyrolysis technique

followed by selenization process in a reductive atmosphere (5 % $H_2$/Ar). Briefly, 0.5 g of multi-walled carbon nanotubes (MWCNTs) with a length of 10–30 mm and an outer diameter of 20–30 nm (obtained from Cheap Tubes Inc., Cambridgeport, USA; purity: >95.0 wt%) and 0.5 g of graphene oxide (GO) nanosheets derived from graphite flakes (Aldrich, <20 μm) *via* a modified Hummer's method, were dispersed in 100 mL of deionized water using ultrasonication for 3 h [51]. The CNTs were purified beforehand using acid treatment, repetitive washing, and freeze-drying, as described in the previous report [27]. Then, 0.1 M of $Co(NO_3)\cdot 6H_2O$ (SAMCHUN, 97.0 %, Mw = 291.02) was added to the above dispersion under continuous stirring, followed by the addition of a 100 mL suspension of 200 nm polystyrene (PS) nanobeads, which acted as porogen. The PS nanobeads were prepared *via* an emulsion polymerization technique. Finally, 2.0 g of polyvinylpyrrolidone (PVP, DAEJUNG, Mw = 40,000) was added as a carbon source and stirred vigorously. The mixture was left undisturbed overnight. The resulting spray solution was then transferred to an ultrasonic atomizer connected to a vertically aligned preheated quartz tube. Ultrasonic atomizer generated aqueous droplets with homogenously dispersed components, which were subsequently fed through the quartz tube maintained at 700 °C, with nitrogen ($N_2$) used as the carrier gas at a flow rate of 10 L $min^{-1}$. The graphical representation of the spray pyrolysis process used in this work is displayed in Scheme S1. The powders obtained after spray pyrolysis underwent a selenization process using excess selenium powder (Se, 200mesh, SAMCHUN, 99.5 %) to produce $H_2Se$ gas. The temperature of the tube furnace was ramped up to 400 °C at a rate of 5 °C $min^{-1}$ and held for 3 h in a reductive atmosphere (5 % of $H_2$/Ar). The resulting powder was designated as P–$CoSe_2$@NGC/rGO−CNT microspheres, with 'P' indicating the porous structure. As a comparison, a sample without rGO and CNT was also prepared under identical synthesis conditions and labeled as P–$CoSe_2$@NGC. Additionally, a non-porous or filled sample without PS nanobeads and any conductive framework (rGO and CNT) was obtained and abbreviated as F–$CoSe_2$@NGC, where 'F' indicates the filled structure. Furthermore, to examine the effect of selenization phase on the electrochemical performance, an oxide phase sample was also synthesized and abbreviated as P–CoO@NGC.

### 2.2. 2.2Materials characterization techniques

The crystal structures of the synthesized powders, namely P–$CoSe_2$@NGC/rGO−CNT, P–$CoSe_2$@NGC, F–$CoSe_2$@NGC, and P–CoO@NGC, were analyzed using a Bruker X-ray diffraction (D2, 2nd generation) instrument employing Cu Kα radiation (λ = 1.5418 Å). Morphological features were examined using field-emission scanning electron microscopy (FE-SEM, Zeiss) and field-emission transmission electron microscopy (FE-TEM) (JEM-2100 F; JEOL). The chemical states and bonding environments of the different elements in the powders were investigated using X-ray photoelectron spectroscopy (XPS) (K-Alpha; Thermo Scientific) equipped with an Al Kα X-ray source. The specific surface area and pore size distribution of the powders were determined using $N_2$ adsorption-desorption isotherms based on the Brunauer–Emmett–Teller (BET) method. Elemental analysis (EA) was employed to quantify the carbon and nitrogen content of the samples. Raman spectroscopy (LabRam, HR800, Horiba Jobin-Yvon) was utilized to study the crystalline characteristics of the carbonaceous products within the prepared microspheres.

### 2.3. Coin cell assembly and electrochemical procedures

The as-prepared microspheres were utilized as multifunctional cathodic interlayers *via* coating onto a commercial Celgard separator. A slurry-casting method was employed for this purpose. The prepared powders, acting as the active material, were mixed with super-P as a conductive agent and polyvinylidene fluoride (PVDF) as a binder in a mass ratio of 7:2:1 in a minimum amount of *N-methyl-2-pyrrolidene* (NMP). The resulting slurry was coated onto a Celgard separator and dried overnight in a hot-air oven preheated at 60 °C. The dried coated slurry was punched into circular discs ($\varphi$ = 19 mm) with an average loading of ~0.37 mg $cm^{-2}$. These discs were transferred to a glove box with controlled $O_2$ and $H_2O$ levels (<0.5 ppm). Additionally, conventional sulfur (S) electrodes were prepared using the identical slurry-casting method. Aluminum foil served as the current collector and the mass ratio of S, super-P, and PVDF was fixed to 7:2:1, respectively. The average loading of S was ~2.0 mg $cm^{-2}$ ($\varphi$ = 14 mm) for conventional electrochemical measurements, resulting in an effective S-content of 56.5 % in the cathode region. However, for high-loading S electrodes, a mass ratio of 8:1:1 was applied, with an active material loading of 3.5 mg $cm^{-2}$ (69 % S) and 4.6 mg $cm^{-2}$ (71 % S). CR2032 coin cells were assembled using the prepared S electrodes as cathodes, metallic Li as the anode, and microporous polypropylene Celgard as a separator. The electrolyte consisted of 1.0 M lithium bis(trifluoromethanesulfonyl) imide with 0.5 M $LiNO_3$ in a blend of 1,3-dioxolane (DOL) and 1,2-dimethoxyethane (DME) in a 1:1 vol ratio. The electrolyte volume was fixed to 40 μL for all the electrochemical tests. The rate capabilities of the assembled cells were measured at various current rates ranging from 0.05 to 2.0 C (1C = 1675 mA h $g^{-1}$) using a WBCS3000 (WonATech) battery cycle at 25 °C. The cycling performance of the cells was evaluated at 0.1, 0.5, and 2.0 C-rate. Cyclic voltammetry (CV) measurements were performed at different voltage scan rates of 0.1–0.5 mV $s^{-1}$. The galvanostatic intermittent titration technique (GITT) was per-formed at a current pulse equivalent to 0.1 C for 30 min followed by a relaxation of 2 h to obtain the quasi-equilibrium reduction potential. All the electrochemical tests were conducted within the voltage range of 1.6–2.8 V. Electrochemical impedance spectroscopy (EIS) data was collected to generate Nyquist plots in the frequency range of 100 kHz–0.01 Hz.

### 2.4. Symmetric cell assembly and polysulfide adsorption tests

To investigate the electrocatalytic effect of the synthesized microspheres, symmetrical cells were assembled. Elemental S powder (S, Sigma-Aldrich, 99.98 %) and $Li_2S$ (≥99 %, Sigma-Aldrich) were dispersed in a ratio of 5:1 in a mixture of 1,3-dioxolane (DOL) and 1,2-dimethoxyethane (DME) (1:1, v/v) at 70 °C overnight, resulting in a dark brown $Li_2S_6$ polysulfide solution. The as-prepared powders were slurry cast onto aluminum foil and used as counter and working electrodes, separated by a Celgard separator. Cyclic voltammetry (CV) plots were obtained for the assembled symmetrical cells with a voltage scan rate of 1.0 mV $s^{-1}$ in a voltage range of −1.5 to 1.5 V. To further analyze the polysulfide trapping potential of the prepared nanostructures, visual demonstration tests were performed. Four glass vials were filled with 1.0 mM of the $Li_2S_6$ solution prepared earlier. Each vial received a dispersion of 5.0 mg of the as-prepared microspheres. A standard polysulfide solution was also prepared separately for comparison. These tests aimed to observe the interaction between the microspheres and polysulfides, providing insights into their polysulfide anchoring capability.

## 3. Results and discussion

### 3.1. Optimization of a suitable three-dimensional nanostructure for durable Li–S batteries

Electrochemical performance is ideally a function of microstructural properties, which means better the nanostructure in terms of conductivity, porosity, and polarity; superior will be the sulfur redox kinetics. To identify the most suitable nanostructure for enhanced electrochemical performance in Li–S cells, a series of different types of powders were synthesized and characterized, as shown in Fig. 1 and S1. The initial precursor powder consisted of porous three-dimensional microspheres composed of NGC-coated cobalt oxide nanocrystals (P–CoO@NGC; P represents "porous"). The FE-SEM micrograph in

Fig. S1a reveals uniformly dispersed microspheres ($\varphi$ = 0.9 μm) with ordered arrays of macropores derived from the PS nanobeads. The X-ray diffraction (XRD) pattern in Fig. S1b shows sharp diffraction peaks corresponding to the CoO phase only. However, when integrated as a multifunctional interlayer with a regular S-electrode, the P–CoO@NGC microspheres exhibited an inferior rate capability, especially at high rates (Figs. S1c and 1j). The NGC layer on the CoO nanocrystals was hypothesized to be insufficient to support fast reaction kinetics. To overcome this issue, a self-supporting framework of highly conductive reduced graphene oxide-carbon nanotubes (rGO−CNT) was introduced during the spray pyrolysis. The rGO−CNT framework not only enhanced the structural integrity of the microspheres but also increased the total conductivity of the nanostructure. The FE-SEM micrograph of the as-sprayed nanostructure (named "P–CoO@NGC/rGO−CNT" microspheres) in Fig. S1d also indicates porous and spherical morphology ($\varphi$ = 1.2 μm). The XRD pattern in Fig. S1e reveals low-intensity diffraction

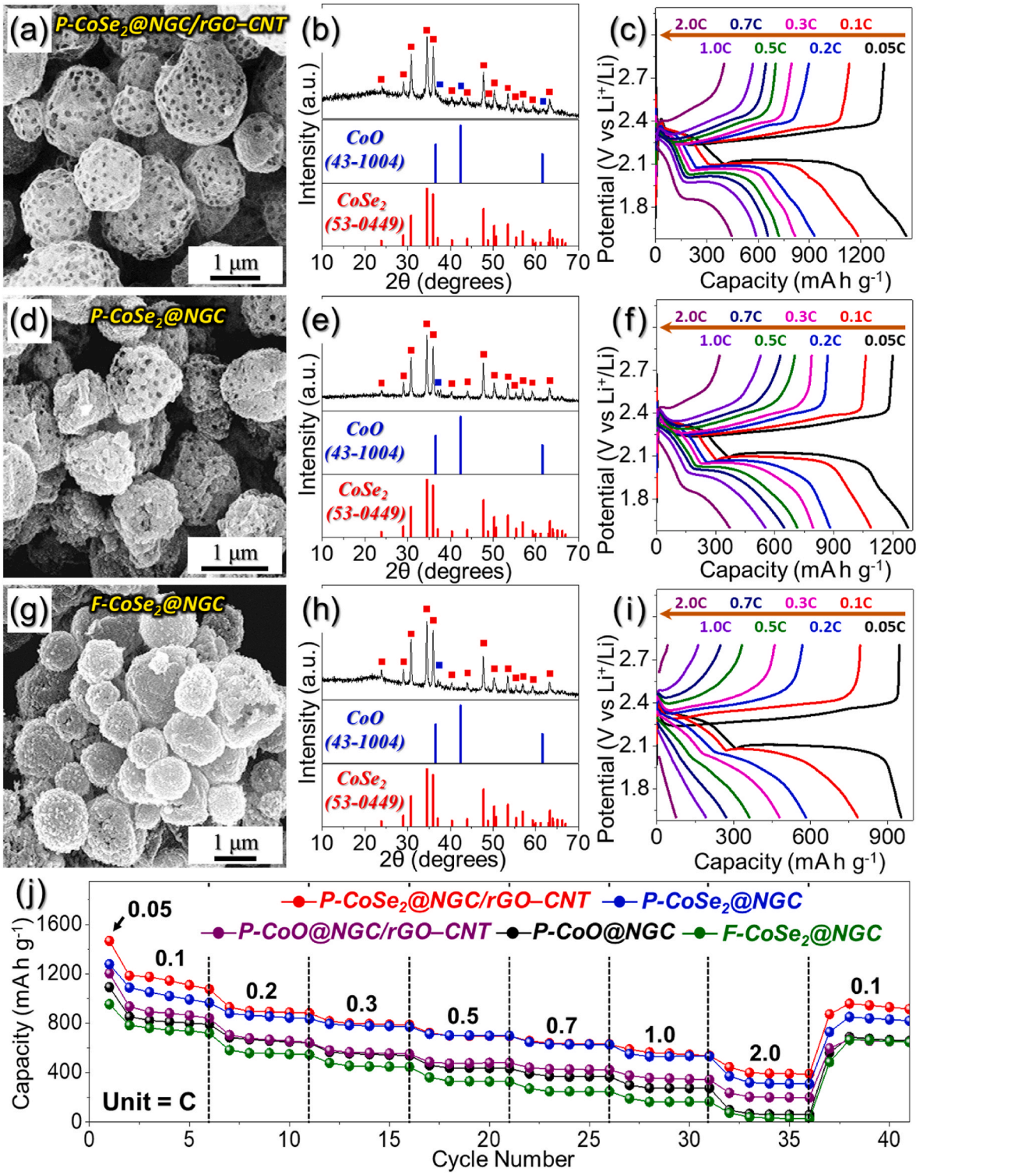


**Fig. 1.** Microstructural information, crystal analysis, and galvanostatic charge−discharge (GCD) profiles for (a–c) P–$CoSe_2$@NGC/rGO−CNT, (d–f) P–$CoSe_2$@NGC, and (g–i) F–$CoSe_2$@NGC along with (j) rate capability tests.

peaks attributed to the CoO phase along with a broad peak located at 2θ = 23° corresponding to the carbonaceous framework. As expected, the rate capability at high C-rates improved significantly (Figs. S1f and 1j). However, to further enhance the rate performance, an additional heat treatment step was introduced, which converts CoO to the $CoSe_2$ phase. The as-sprayed P–CoO@NGC/rGO−CNT powder was selenized at 400 °C for 3 h in a reducing atmosphere (5 % $H_2$/Ar), leading to the transformation of the CoO phase to the respective $CoSe_2$ phase with trace amounts of the oxide phase. Notably, the high polarity of transition metal selenides (TMSes), owing to the presence of numerous active sulfiphilic sites, facilitates the efficient capture of the LiPSs species and improves the electrochemical performance considerably [7]. The resulting selenized sample, denoted as P–$CoSe_2$@NGC/rGO−CNT, also displayed a spherical and porous morphology (Fig. 1a). The XRD pattern in Fig. 1b shows sharp peaks indexed to the orthorhombic phase of the $CoSe_2$ crystal structure. However, a few low-intensity peaks corresponding to the oxide phase remain. Importantly, the GCD profiles (Fig. 1c) and rate capability results (Fig. 1j) improved drastically at all C-rates (0.05–2.0 C), indicating kinetically favored redox processes. These results confirm that the phase change (oxide → selenide) and microstructural improvements have a substantial effect on the electrochemical performance of Li–S cells. In comparison, two additional samples, namely P–$CoSe_2$@NGC and F–$CoSe_2$@NGC (F representing "filled"), with lower microstructural merits compared to the P–$CoSe_2$@NGC/rGO−CNT microspheres, firmly support the above reasoning. The P–$CoSe_2$@NGC (without rGO−CNT framework) and F–$CoSe_2$@NGC (without rGO−CNT and macropores) powders exhibit substandard rate capabilities (Fig. 1f, i, and 1j), even though both displayed selenide phases (Fig. 1e and h). Therefore, based on the above results, we anticipate that the P–$CoSe_2$@NGC/rGO−CNT sample, with its favorable structure (owing to the presence of a self-supporting rGO−CNT framework and macropores) and phase stability (highly polar selenide phase), will provide superior electrochemical performance for more durable and practical Li–S batteries.

### 3.2. Physical characterizations of the as-prepared powders

A systematic examination was conducted to analyze the microstructural and phase properties of the nanostructures prepared at each step. Fig. 2 shows the morphology and crystal structure of the powder collected after spray pyrolysis. The spray solution consisted of Co salt, GO nanosheets, CNTs, PS nanobeads ($\varphi$ = 200 nm), and PVP as the carbon source. The FE-SEM micrographs in Fig. 2a and b shows uniformly dispersed non-aggregated microspheres with an average diameter of ~1.2 μm. Additionally, ordered arrays of macropores derived from the PS nanobeads were also observed. The cross-sectional image in

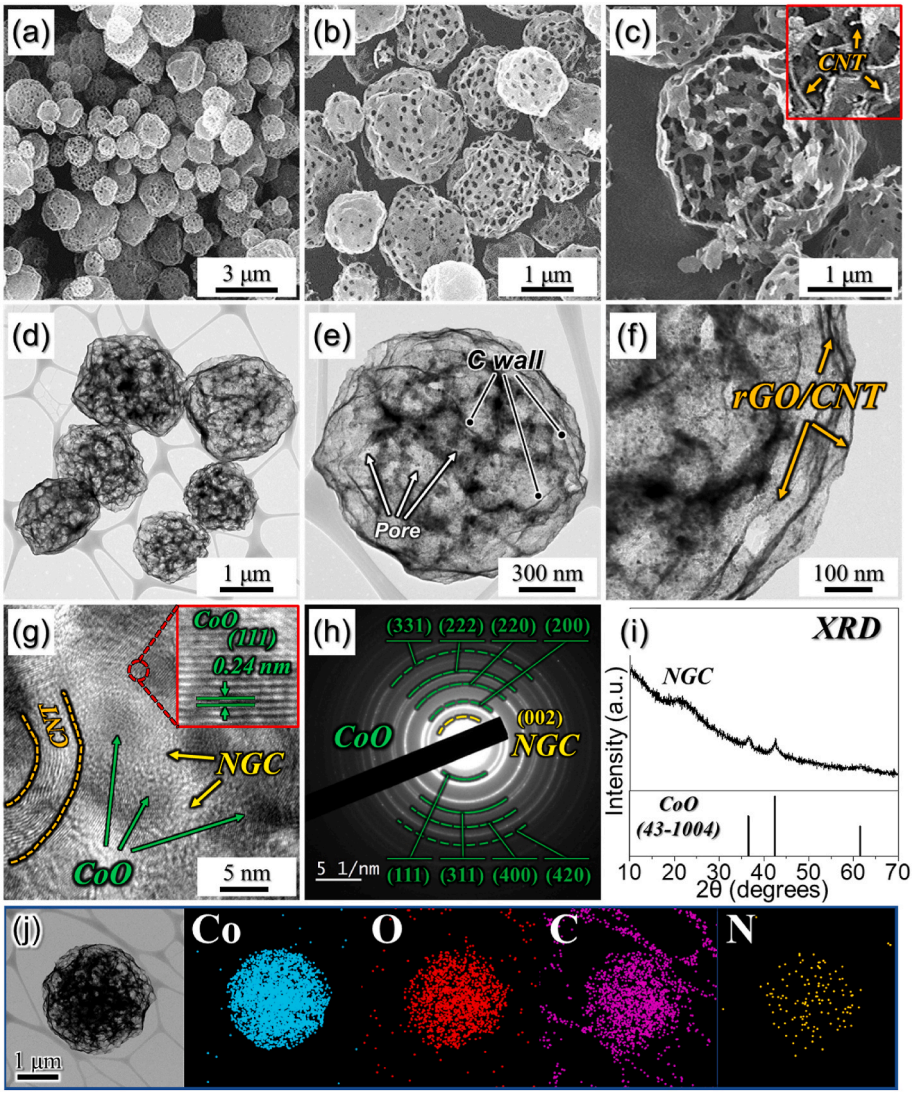


**Fig. 2.** Physical characterizations of the as-sprayed P–CoO@NGC/rGO−CNT microspheres: (a–c) FE-SEM images, (d–f) TEM images, (g) HR-TEM image, (h) SAED pattern, (i) XRD pattern, and (j) elemental dot mapping images.

Fig. 2c also indicates the macropore-derived porous nanostructure. During spray pyrolysis, the PS nanobeads were completely decomposed, leaving behind macropores. However, the pore size decreased from 200 to ~100 nm owing to microsphere shrinkage during pyrolysis. The TEM image in Fig. 2d confirms the well-dispersed spherical morphology of the sample. Moreover, the high-magnification TEM image (Fig. 2e) reveals the presence of macropores (highlighted by arrows) distributed within the carbonaceous matrix (marked as the C-wall). The carbonaceous species primarily consisted of the rGO–CNT framework, as shown in Fig. 2f (highlighted by arrows). The rGO–CNT framework not only provides structural integrity to the nanostructure but also enhances its total electronic conductivity. Fig. 2g displays a high-resolution TEM (HR-TEM) image showing the uniformly distributed and well-grafted CoO nanocrystals (~3.0 nm). The presence of a CNT matrix was also observed, along with the lattice fringes separated by a distance of 0.24 nm corresponding to the (111) diffraction plane of the CoO phase. The selected-area electron diffraction (SAED) pattern in Fig. 2h confirms the CoO crystal structure with well-fitted diffraction rings. An additional diffraction ring attributed to the PVP-derived NGC species, i.e., the (002) plane, is also observed. The XRD pattern in Fig. 2i supports the SAED results, displaying low-intensity peaks indexed to the CoO crystal phase along with a broad diffraction peak centered at $2\theta = 23^{\circ}$, indicating the presence of a carbonaceous framework in the nanostructure. The elemental dot mapping images in Fig. 2j show a uniform distribution of

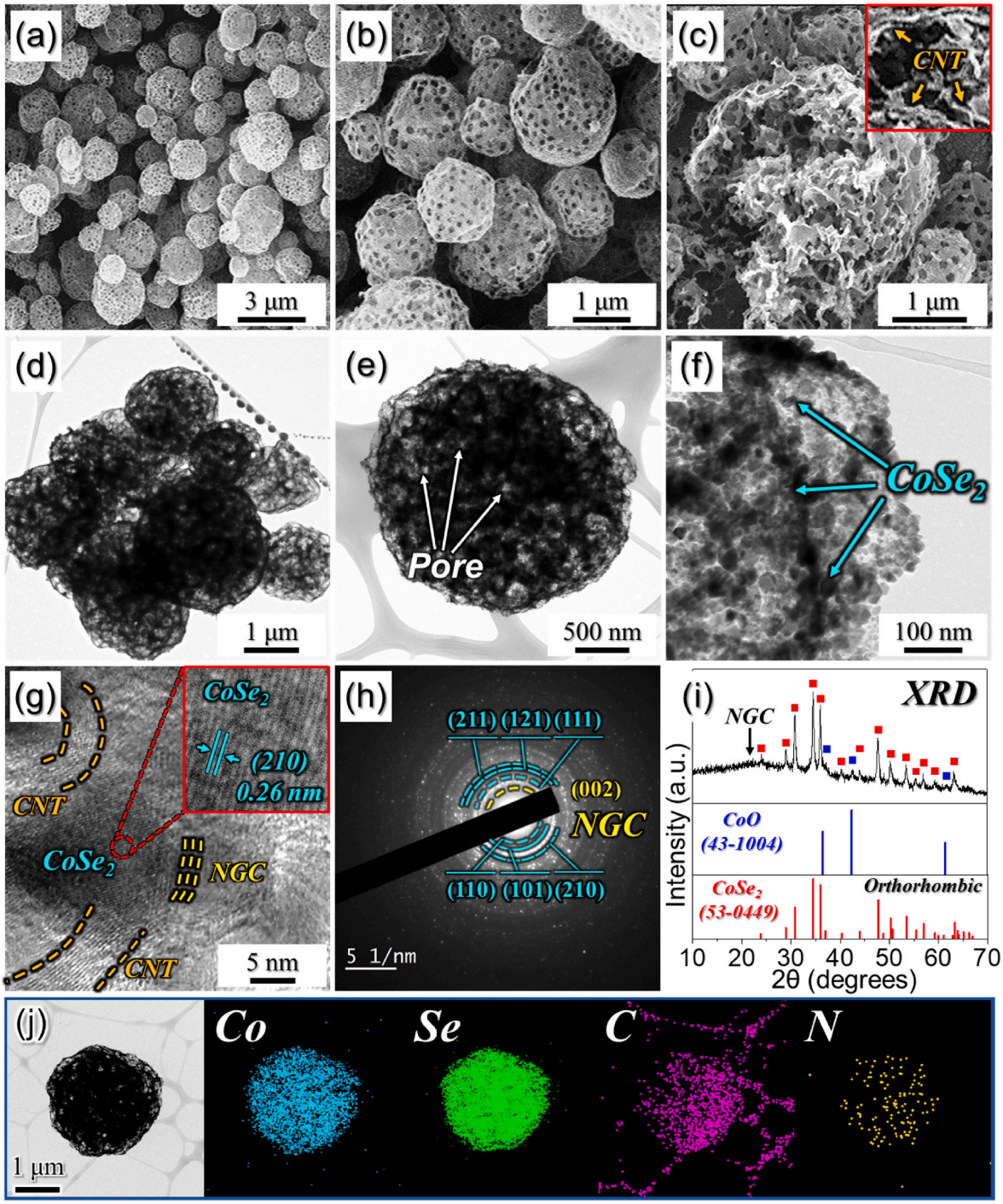


**Fig. 3.** Physical characterizations of P–$CoSe_2$@NGC/rGO–CNT microspheres: (a–c) FE-SEM images, (d–f) TEM images, (g) HR-TEM image, (h) SAED pattern, (i) XRD pattern, and (j) elemental dot mapping images.

Co, O, C, and N throughout the prepared nanostructures. Therefore, the above results confirm the formation of three-dimensional porous and highly conductive microspheres comprising well-grafted N-doped graphitic carbon (NGC)-coated CoO nanocrystals within the self-supporting rGO–CNT carbonaceous framework ("P–CoO@NGC/rGO–CNT" microspheres).

The P–CoO@NGC/rGO–CNT microspheres obtained from the spray process underwent a selenization process, wherein the furnace temperature was gradually raised to 400 °C at a ramp rate of 5 °C $min^{-1}$ and maintained for 3 h under a reducing atmosphere (5 % $H_2$/Ar). The resulting morphological and crystal structure changes are shown in Fig. 3. The FE-SEM micrographs in Fig. 3a and b confirm that the selenized powder retained its uniformly dispersed spherical morphology, with an average diameter of ~1.2 μm. Furthermore, the ordered arrays of macropores remained intact. The fractured FE-SEM image in Fig. 3c also suggests the presence of macropores in the microspheres. The TEM images in Fig. 3d and e validate the FE-SEM findings and reveal the formation of a porous three-dimensional nanostructure. A closer examination of Fig. 3f reveals the presence of well-embedded, non-agglomerated nanocrystals within the rGO–CNT carbonaceous framework. The carbon species play a crucial role in facilitating the controlled growth and crystallization of CoO nanocrystals into their respective selenide phases. The HR-TEM image in Fig. 3g reveals the presence of a CNT matrix and lattice fringes separated by a distance of 0.26 nm, which corresponds to the (210) diffraction plane of the $CoSe_2$ crystal structure. The SAED pattern in Fig. 3h confirms the presence of diffraction rings associated with the orthorhombic crystal structure of the $CoSe_2$ phase. A diffraction ring corresponding to the (002) plane of NGC was also observed. Notably, the presence of the NGC layer on the $CoSe_2$ nanocrystals significantly enhances the electronic conductivity by serving as the primary transport pathway for fast and continuous electron transmission. These electrons were subsequently transferred to the secondary pathways formed by the rGO–CNT framework. The CNTs play a crucial role as bridging links between successive graphene nanosheets, ensuring the uninterrupted transmission of charge carriers. The XRD pattern shown in Fig. 3i closely correlates with the SAED pattern, displaying sharp and well-indexed peaks corresponding to the orthorhombic phase of the $CoSe_2$ crystal structure, along with a broad peak indicating the presence of NGC. Moreover, trivial traces of the CoO-phase are also observed. The elemental dot mapping images provide compelling evidence of the formation of the $CoSe_2$ crystal structure, revealing a uniform distribution of Co and Se within the N-doped carbonaceous framework. In other words, the resulting nanostructure comprised uniformly distributed NGC-coated $CoSe_2$ nanocrystals entangled within a three-dimensional porous and highly conductive rGO–CNT framework (P–$CoSe_2$@NGC/rGO–CNT).

Based on the above discussion, we summarize the detailed formation mechanism of the P–$CoSe_2$@NGC/rGO–CNT microspheres in Scheme 1.

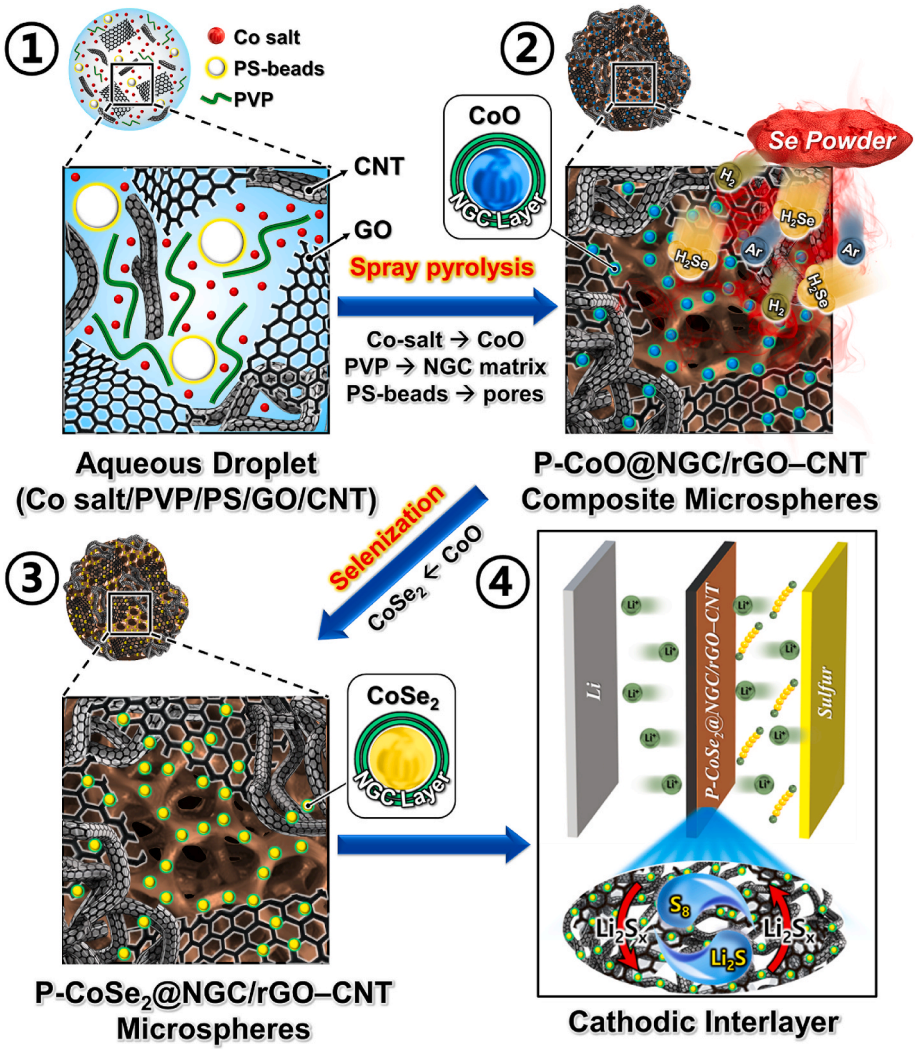


**Scheme 1.** Schematic illustration of the formation mechanism of P–$CoSe_2$@NGC/rGO–CNT microspheres *via* (① and ②) facile spray pyrolysis technique followed by (③) selenization at 400 °C for 3 h, and (④) their applicability as multifunctional cathodic interlayer.

Initially, aqueous droplets were formed using an ultrasonic nebulizer unit. These droplets consist of a uniformly dispersed Co salt, PVP as the carbon source, a suspension of PS nanobeads ($\varphi$ = 200 nm), GO nanosheets, and CNT, as depicted in Scheme 1-①. Subsequently, the droplets passed through a vertically placed quartz tube that had been preheated to 700 °C, with flowing $N_2$ as the carrier gas. This process resulted in the drying of the droplets and their transformation into a more compact form. Additionally, the Co salt was converted to the CoO phase, whereas PVP decomposed to form the C-matrix (Scheme 1-②). Simultaneously, the PS nanobeads underwent a complete thermal breakdown, leading to the formation of macropores that were uniformly distributed throughout the microspheres. Moreover, the C matrix gradually transformed into a more uniform NGC layer, catalyzed by the presence of Co species. This NGC-coated layer acts as the primary transport pathway for efficient electron transport, ensuring fast and uninterrupted electron passage. The rGO−CNT framework served as the secondary pathway for electron transmission. The as-sprayed powders then underwent a selenization process at 400 °C for 3 h, with a ramp rate of 5 °C $min^{-1}$, under a reducing atmosphere (5 % $H_2$/Ar). Excess selenium powder was used to generate $H_2Se$ gas. During the selenization process, the CoO-phase was converted into a selenide phase with well-embedded NGC-coated $CoSe_2$ nanocrystals within the rGO−CNT conductive framework (Scheme 1-③). The obtained P–$CoSe_2$@NGC/rGO−CNT microspheres were used as multifunctional cathodic interlayers by coating them onto a commercial Celgard separator (Scheme 1-④). The functional interlayer acts as a catalytic barrier to weaken the polysulfide diffusion thus ensuring high active-material utilization which subsequently resulted in enhanced electrochemical performance.

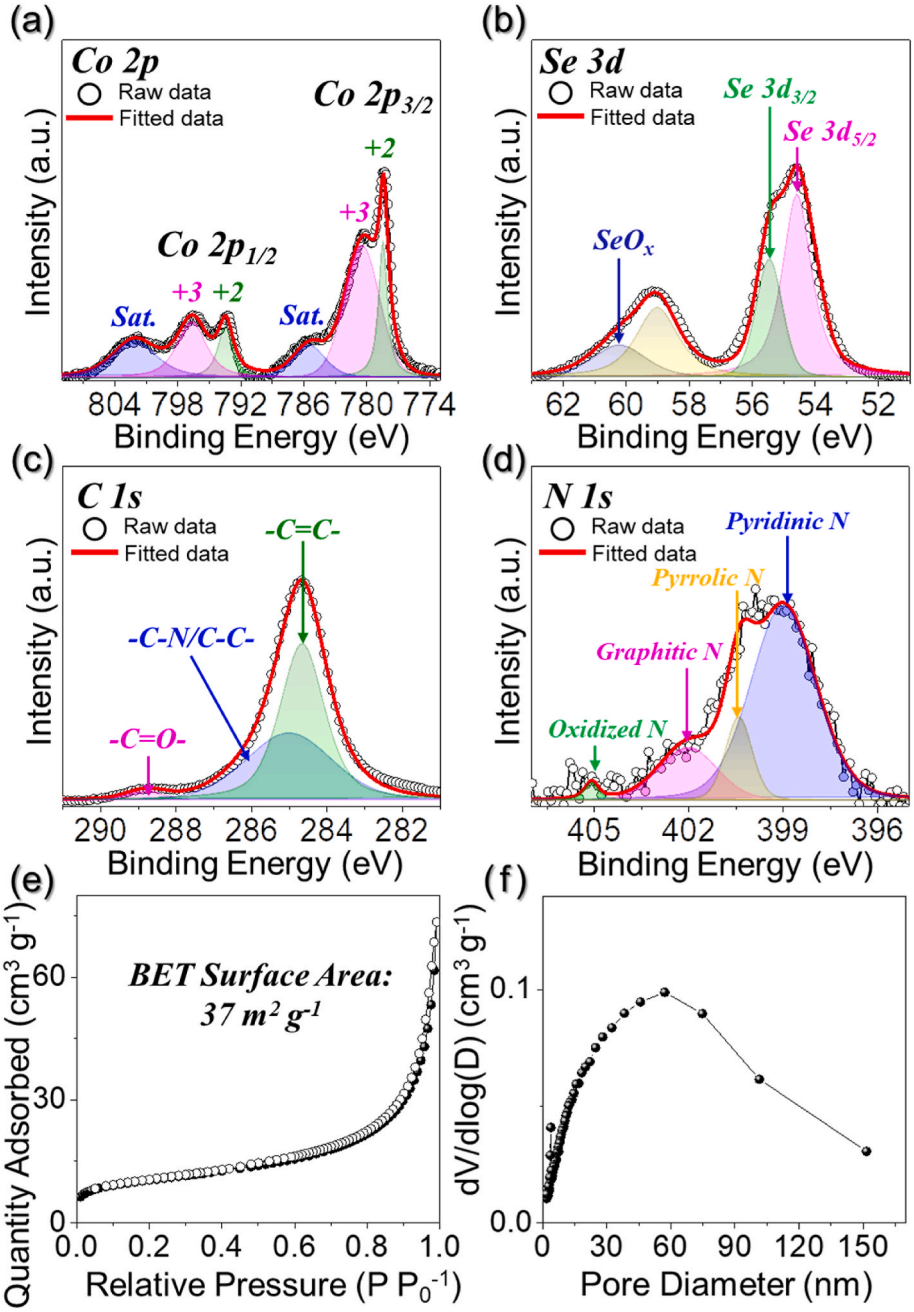


**Fig. 4.** XPS, surface area, and pore size characteristics of P–$CoSe_2$@NGC/rGO−CNT microspheres obtained after selenization at 400 °C for 3 h: (a) Co 2*p* XPS spectrum, (b) Se 3*d* XPS spectrum, (c) C 1*s* XPS spectrum, (d) N 1*s* XPS spectrum, (e) $N_2$ adsorption-desorption isotherms, and (f) BJH desorption pore-size distribution.

The chemical state of various elements in the P–$CoSe_2$@NGC/rGO–CNT powder was examined using XPS. The survey scan in Fig. S2 revealed distinct photoelectron peaks corresponding to the Co 2*p*, O 1*s*, N 1*s*, C 1*s*, and Se 3*d* orbitals. In the high-resolution Co 2*p* signal (Fig. 4a), two spin-orbit doublets, Co $2p_{3/2}$ and Co $2p_{1/2}$, are observed at binding energies of 778.3 and 793.4 eV, respectively [54–56]. Additionally, the deconvolution spectra of the Co $2p_{3/2}$ and Co $2p_{1/2}$ orbitals indicate the presence of +3 and + 2 oxidation states, consistent with previous reports [26,57]. The two shake-up peaks, labeled "*Sat.*," correspond to antibonding orbitals between the Co and Se atoms [58]. The high-resolution Se 3*d* XPS spectrum (Fig. 4b) shows well-fitted photoelectron peaks for Se $3d_{5/2}$ and Se $3d_{3/2}$ at binding energies of 54.5 and 55.4 eV, respectively, indicating the interaction of Se with metallic Co in $CoSe_2$ [58,59]. Furthermore, the peak at 59.0 eV is attributed to the Co 3*p* species on the surface, whereas the peak at 60.2 eV is related to the surface oxidation of Se (Se–O bond), in agreement with previous reports [60]. The C 1*s* spectrum (Fig. 4c) exhibits three well-fitted peaks centered at 284.6, 286.5, and 288.7 eV, corresponding to the –C═C-, -C-N/C–C-, and –C═O- bonding species, respectively [61–63]. The pronounced intensity of the –C═C- peak confirms the presence of carbonaceous species in the prepared nanostructure [64]. Moreover, the -C-N/C–C- peak indicates N-doping in the carbon framework, promoting enhanced electronic conductivity owing to the high electronegativity of the N atom compared to the C atom [65,66]. The high-resolution N 1*s* spectrum was deconvoluted into four well-fitted peaks located at 398.9, 400.3, 402.0, and 405.0 eV, corresponding to pyridinic N, pyrrolic N, graphitic N, and oxidized N, respectively [67]. To quantify the N-doping in the carbonaceous framework, elemental analysis (EA) was performed (Table S1), and the obtained N content was observed ~0.75 wt%, thus confirming the presence of an N-doped carbon framework. The N-doping is facilitated by the N-rich organic units in the PVP polymer. Additionally, the carbon content in the P–$CoSe_2$@NGC/rGO–CNT nanostructure was observed to be 8.8 wt%. Raman analysis was conducted to examine the crystalline nature of the carbonaceous species in the P–$CoSe_2$@NGC/rGO–CNT microspheres (Fig. S3). Moreover, the Raman spectrum of the P–CoO@NGC/rGO–CNT sample was also obtained for better comparison (Fig. S3a). The Raman spectrum of the P–$CoSe_2$@NGC/rGO–CNT (Fig. S3b) exhibited the well-known D- and G-band signatures at 1138 and 1582 $cm^{-1}$, respectively [68]. The relative intensity ratio of the D- and G-bands ($I_D/I_G$) indicates the crystalline nature of the carbonaceous species in the prepared microspheres. An $I_D/I_G$ value of 0.98 confirms the crystalline nature of the carbonaceous products. In addition, the well-resolved peak at 669 $cm^{-1}$ is attributed to the $A_{1g}$ mode of the Co–Se bonds in $CoSe_2$ [69]. The two low-intensity peaks located at 463 and 506 $cm^{-1}$ are related to the trace amounts of Co–O bonds, primarily resulting from surface oxidation [70]. Furthermore, the Raman peak centered at 164 $cm^{-1}$ is assigned to the stretching mode of the Se–Se bond in $CoSe_2$ [69]. The surface area and pore size distribution of the P–$CoSe_2$@NGC/rGO–CNT microspheres were examined using $N_2$ adsorption-desorption isotherms, as shown in Fig. 4e and f, respectively. The nanostructure exhibited a surface area of 37 $m^2\ g^{-1}$ (Fig. 4e), predominantly due to the macropores derived from the PS nanobeads that were uniformly distributed within the microsphere structure. The pore-size distribution curve in Fig. 4f also shows a broad peak centered at 57 nm, confirming the presence of macropores. Importantly, the existence of macropores in the nanostructure not only facilitates the smooth diffusion of charged species *via* the shortening of the effective diffusion length but also provides enough space to absorb unwanted volume fluctuations along with the efficient electrolyte percolation.

The phase and morphological superiorities of the P–$CoSe_2$@NGC/rGO–CNT microspheres were further confirmed by synthesizing consecutive comparison samples. The spray solution used for the comparison samples included Co salt, PS nanobeads, and PVP in deionized water (without rGO and CNT). For one comparison sample, the as-sprayed powder was utilized without further heat treatment and is abbreviated as P–CoO@NGC microspheres. In contrast, the second comparison sample was obtained *via* an additional heat-treatment step (selenization) after spray pyrolysis in a reductive atmosphere (5 % $H_2$/Ar) at 400 °C and abbreviated as P–$CoSe_2$@NGC microspheres. The morphology and phase information of the as-sprayed P–CoO@NGC microspheres is presented in Fig. S4. The FE-SEM micrographs in Figs. S4a–c reveals the formation of three-dimensional porous microspheres ($\varphi$ = 1.1 μm) with well-formed macropores derived from PS nanobeads distributed throughout the microsphere structure (Fig. S4c). The TEM images (Figs. S4d–f) validate the FE-SEM results, confirming the presence of porous microspheres comprising well-embedded CoO nanocrystals in the PVP-derived NGC matrix (Fig. S4f). Notably, the absence of the rGO–CNT carbonaceous framework resulted in uncontrolled growth and crystallization, leading to larger CoO nanocrystals (~6.0 nm). The high-resolution TEM (HR-TEM) image in Fig. S4g reveals lattice fringes separated by 0.24 nm, corresponding to the (111) diffraction plane of the CoO phase. The SAED pattern shown in Fig. S4h displays diffraction rings that are well-indexed to the CoO phase, along with the (002) diffraction plane corresponding to the NGC matrix. The XRD pattern in Fig. S4i is consistent with the SAED pattern, indicating sharp peaks associated entirely with the CoO phase. The elemental dot-mapping images shown in Fig. S4j demonstrate the uniform dispersion of Co, O, C, and N, confirming the formation of CoO nanocrystals confined within the N-doped carbonaceous species.

The as-sprayed P–CoO@NGC powder was selenized to obtain P–$CoSe_2$@NGC microspheres, and the physical characterization results are summarized in Fig. S5. The FE-SEM images in Figs. S5a–c demonstrate that the spherical shape remained intact after selenization, along with the preserved porous structure. However, the uncontrolled growth of the $CoSe_2$ nanocrystals (Fig. S5c) during the heat treatment led to the formation of large crystals. TEM images in Figs. S5d–f firmly support the FE-SEM results, showing non-agglomerated microspheres with slightly porous nanostructures (Fig. S5e), along with large $CoSe_2$ nanocrystals that predominantly occupied the available space (Fig. S5f). The formation of large $CoSe_2$ nanocrystals was due to the absence of the rGO–CNT species, which possibly restricted grain growth and crystallization. The HRTEM image (Fig. S5g) also indicates lattice fringes separated by 0.26 nm, corresponding to the (210) crystal plane of the $CoSe_2$ phase. Moreover, the presence of an NGC layer on the $CoSe_2$ nanocrystals is also evident. The SAED (Fig. S5h) and XRD patterns (Fig. S5i) are consistent with the aforementioned results, revealing the existence of an orthorhombic $CoSe_2$ crystal structure. The elemental dot-mapping images in Fig. S5j show a uniform dispersion of Co, Se, C, and N, suggesting the formation of well-confined $CoSe_2$ nanocrystals within the N-doped carbonaceous species. The carbon and nitrogen percentages in the P–$CoSe_2$@NGC microspheres are presented in Table S1 and indicate the presence of nitrogen-doped carbonaceous species in the form of NGC. However, the low carbon content (4.6 wt%) was mainly attributed to the absence of the rGO–CNT framework. Finally, a filled sample (F–$CoSe_2$@NGC) was also prepared using a spray solution consisting solely of the Ni salt and PVP in deionized water (without rGO, CNT, or PS nanobeads), followed by selenization. The morphological and crystal structure changes in the as-sprayed and selenized powders are presented and discussed in Figs. S6 and S7, respectively.

### 3.3. Electrochemical performance of the prepared nanostructures

The prepared P–$CoSe_2$@NGC/rGO–CNT microspheres were applied as a multifunctional cathodic interlayer on a commercial Celgard separator to enhance the electrochemical performance of Li–S cells. The coated and pristine separators were analyzed in advance, and the results are summarized in Fig. S8. A cross-sectional image of the P–$CoSe_2$@NGC/rGO–CNT-coated separator in Fig. S8a shows a uniform coating of the nanostructure on the separator, with a thickness of ~10 μm. The magnified FE-SEM image shown in Fig. S8b reveals a uniform coating of the P–$CoSe_2$@NGC/rGO–CNT microspheres and super-P on

the separator surface. The FE-SEM micrograph of the pristine Celgard separator in Fig. S8c shows submicron openings that allow the diffusion of charged species and electrolyte during the electrochemical process. CR2032-type coin cells were assembled using regular S electrodes, Li anodes, and coated separators as multifunctional interlayers to evaluate the improvement in electrochemical performance. Notably, considering the separator loading, the effective sulfur content in the cathode region was *ca.* 56.5 %. CV tests were conducted on Li–S cells featuring P–$CoSe_2$@NGC/rGO−CNT, P–$CoSe_2$@NGC, F–$CoSe_2$@NGC, and P–CoO@NGC microspheres as coated separators, as shown in Fig. 5a. During the initial cathodic scan at 0.1 mV $s^{-1}$, all the cells exhibited a typical two-step sulfur reduction process. The reduction peak labeled "R1" corresponded to the reduction of elemental sulfur to highly soluble higher or middle-order LiPSs ($Li_2S_x$, $4 \leq x \leq 8$), while the reduction peak marked "R2" is associated with a further reduction to the insoluble solid $Li_2S_2/Li_2S$ state [71]. The anodic scan featured an oxidation peak labeled "O," indicating the single-step oxidation of $Li_2S_2/Li_2S$ back to elemental sulfur *via* $Li_2S_x$ [72]. Among the assembled cells, the Li–S cell with the P–$CoSe_2$@NGC/rGO−CNT-coated separator exhibited sharp and high-intensity reduction peaks, suggesting improved redox kinetics and better utilization of the active material. This observation is further supported by the individual redox peak voltage values and the corresponding voltage polarization (voltage difference between R1 and O), as shown in Fig. 5b. The Li–S cell paired with the P–$CoSe_2$@NGC/rGO−

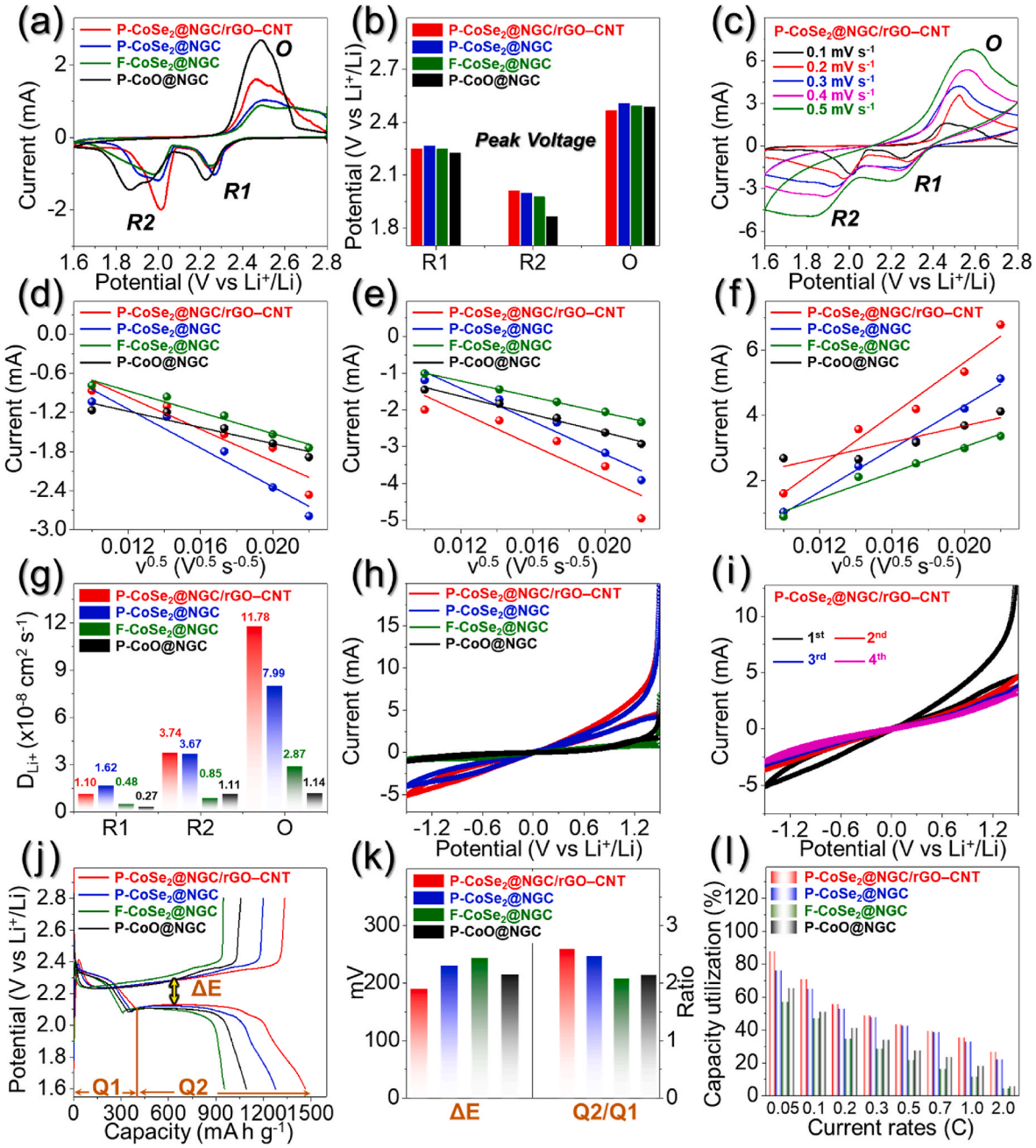


**Fig. 5.** (a) CV profiles of Li–S cells featuring different coated separator arrangement at 0.1 mV $s^{-1}$, (b) redox peak voltage comparison obtained from CV graphs, (c) CV profile at various voltage scan rates, (d–f) peak current *vs.* square root of the voltage scan rate plots for reduction and oxidation peaks, (g) lithium-ion diffusion coefficient ($D_{Li}^{+}$) values comparison, (h) comparison of electrocatalytic activity of as-prepared nanostructures using CV profiles from symmetric cells at a scan rate of 1.0 mV $s^{-1}$, (i) four initial CV scans for symmetric cell featuring P–$CoSe_2$@NGC/rGO–CNT microspheres as counter and working electrode, (j) GCD voltage profiles of different coated separator arrangements at 0.05 C, (k) ΔE and Q2/Q1 comparison for different coated separator, and (l) capacity utilization at various C-rates.

CNT-coated separator exhibited the lowest polarization potential (ΔV = 216 mV) compared to P–$CoSe_2$@NGC (ΔV = 241 mV), F–$CoSe_2$@NGC (ΔV = 244 mV), and P–CoO@NGC (ΔV = 261 mV) coated separators. The five initial CV profiles shown in Fig. S9 display well-overlapping curves, indicating highly reversible and kinetically favored redox processes within the cells. To further demonstrate the improved redox kinetics in Li–S cells featuring the P–$CoSe_2$@NGC/rGO−CNT-coated separator compared to the other cells, CV curves at different voltage scan rates ranging from 0.1 to 0.5 mV $s^{-1}$ were obtained and analyzed (Fig. 5c). The shapes of the CV curves clearly indicate that the redox processes involved only S and $Li_2S$ and exhibited typical redox signatures, even at a high voltage scan rate of 0.5 mV $s^{-1}$. However, at high scan rates, the current intensity increases with increasing voltage hysteresis. The CV curves for the Li–S cells with the P–$CoSe_2$@NGC, F–$CoSe_2$@NGC, and P–CoO@NGC-coated separators (Fig. S10) exhibited similar redox characteristics, but the current intensity and voltage hysteresis varied, suggesting different extents of the redox reaction. The diffusion kinetics within the assembled cells were evaluated using the Randles-Sevcik equation [18]:

$$I_p = 2.69\times10^5 n^{1.5} A\, D_{Li^+}^{0.5}\, C_{Li}\, \nu^{0.5} \quad (1)$$

where all parameters have typical meanings. The Li-ion diffusion coefficient ($D_{Li}^{+}$) was calculated for all Li–S cells using the slope from the $I_p$ vs. $\nu^{0.5}$ curves for the three redox peaks (i.e., R1, R2, and O), as shown in Fig. 5d–f. The obtained $D_{Li}^{+}$ values are presented in Fig. 5g. The highest $D_{Li}^{+}$ values for the Li–S cell featuring P–$CoSe_2$@NGC/rGO−CNT, compared to those with P–$CoSe_2$@NGC, F–$CoSe_2$@NGC, and P–CoO@NGC-coated separators, indicate improved reaction kinetics inside the cell. This improvement is primarily attributed to the robust nanostructure engineering strategy, which ensures structural integrity and promotes synergetic effects between various components. For instance, the NGC coating that surrounds the $CoSe_2$ nanocrystals acts as a primary electron pathway, facilitating fast electron transfer and supporting the smooth catalytic conversion of the trapped polysulfide species. Additionally, the self-supporting rGO−CNT framework with entangled CNTs bridging the graphene nanosheets, behave as secondary pathways for longitudinal and vertical electron transport during the electrochemical process. The above results were further supported by examining the symmetric cell configurations to explore the electrocatalytic conversion effect of all the prepared nanostructures. The initial CV curve within the voltage window of −1.5 to 1.5 V (Fig. 5h) clearly indicates that the symmetric cell featuring the P–$CoSe_2$@NGC/rGO−CNT microspheres as both counter and working electrode exhibits the highest current intensity, supporting its effective electrocatalytic behavior towards LiPSs. In contrast, symmetric cells with P–$CoSe_2$@NGC, F–$CoSe_2$@NGC, and P–CoO@NGC displayed weak electrocatalytic activity towards LiPSs. Moreover, the four consecutive CV cycles in Fig. 5i almost overlap, indicating the repeated catalytic conversion capability of the P–$CoSe_2$@NGC/rGO−CNT microspheres. This is primarily due to the presence of well-grafted $CoSe_2$ nanocrystals, which act as active chemisorption sites for the efficient anchoring and electrocatalytic conversion of the trapped polysulfide species, thus ensuring high utilization of the active material. Overall, the above results demonstrate the enhanced electrochemical performance of the P–$CoSe_2$@NGC/rGO−CNT microspheres compared to those with P–$CoSe_2$@NGC, F–$CoSe_2$@NGC, and P–CoO@NGC, owing to the nanostructure advantages, such as robust structure, porous framework, highly conductive skeleton, and the presence of polar chemisorption sites.

The galvanostatic charge-discharge (GCD) voltage profiles were plotted at 0.05 C for all Li–S cells with various coated separators, as shown in Fig. 5j. These profiles show two discharge voltage plateaus and a sloping charging profile, indicating multistep sulfur redox processes, which is consistent with the CV curves in Fig. 5a. However, the lengths of the redox voltage plateaus differed among the arrangements, suggesting uneven redox kinetics inside the cells. Among the assembled Li–S cells, the cell featuring the P–$CoSe_2$@NGC/rGO−CNT-coated separator exhibited the longest redox voltage plateaus and the lowest voltage polarization (ΔE) between the second reduction and oxidation voltage plateaus. The calculated ΔE values are summarized in Fig. 5k, indicating that the P–$CoSe_2$@NGC/rGO−CNT-coated separator has the lowest polarization value (ΔE = 190 mV) compared to the P–$CoSe_2$@NGC (ΔE = 230 mV), F–$CoSe_2$@NGC (ΔE = 243 mV), and P–CoO@NGC (ΔE = 215 mV) coated separators. Additionally, two independent variables, namely, Q1 and Q2, along with their relative ratio (i.e., Q2/Q1), were also measured. The quantity Q1 is related to the amount of the LiPSs formed and their diffusion towards the anode and was measured as the discharge capacity value (theoretical value = 419 mA h $g^{-1}$) exhibited by the first discharge plateau and sloppy region [73]. Likewise, Q2 is associated with the efficient conversion of LiPSs to $Li_2S$ and is measured as the discharge capacity value (theoretical value = 1256 mA h $g^{-1}$) exhibited by the second discharge plateau and subsequent sloppy region [74]. The Q2/Q1 ratio (theoretical value = 3) indicates the electrocatalytic conversion capability of the nanostructure [73]. Correspondingly, a higher Q2/Q1 value guarantees a better catalytic conversion of the trapped polysulfide species. The cell featuring the P–$CoSe_2$@NGC/rGO−CNT-coated separator exhibited the highest Q2/Q1 ratio (2.59) compared to the P–$CoSe_2$@NGC (Q2/Q1 = 2.47), F–$CoSe_2$@NGC (Q2/Q1 = 2.07), and P–CoO@NGC (Q2/Q1 = 2.14) coated separators. This implies better electrocatalytic activity of the P–$CoSe_2$@NGC/rGO−CNT microspheres towards lithium polysulfide species and, hence, higher active material utilization. Correspondingly, the P–$CoSe_2$@NGC/rGO−CNT, P–$CoSe_2$@NGC, F–$CoSe_2$@NGC, and P–CoO@NGC-coated separators exhibited initial discharge capacities of 1465 (87.4 % of the theoretical value), 1276 (76.1 % of the theoretical value), 953 (56.8 % of the theoretical value), and 1091 (65.1 % of the theoretical value) mA h $g^{-1}$, respectively. The highest discharge capacity of the P–$CoSe_2$@NGC/rGO−CNT-coated separator is a clear evidence of kinetically favored reaction processes derived from a conductive, porous, and polar framework, which eventually resulted in high active material utilization. Rate capability tests, along with their respective GCD profiles (Fig. 1 and S1) for Li–S cells utilizing different coating arrangements, confirmed the above results. The cell with the P–$CoSe_2$@NGC/rGO−CNT (Fig. 1c) and P–$CoSe_2$@NGC (Fig. 1f)-coated separators exhibited well-distinguished charge−discharge voltage plateaus even at a high C-rate of 2.0 C. However, the difference in the voltage plateau length resulted in high discharge capacity values for the P–$CoSe_2$@NGC/rGO−CNT-coated separator cell at all C-rates, as shown in Fig. 1j. For instance, initial discharge capacities of 1465, 1183, 930, 816, 721, 656, 588, and 444 mA h $g^{-1}$ were obtained at 0.05, 0.1, 0.2, 0.3, 0.5, 0.7, 1.0, and 2.0 C, respectively, for the P–$CoSe_2$@NGC/rGO−CNT-coated separator cell compared to 1276, 1087, 880, 794, 714, 647, 551, and 370 mA h $g^{-1}$ at identical C-rates for the P–$CoSe_2$@NGC-coated separator cell. In contrast, the F–$CoSe_2$@NGC and P–CoO@NGC-coated separators exhibited low discharge capacities of 953/1091, 783/852, 581/685, 478/566, 361/459, 270/392, 191/298, and 72/98 mA h $g^{-1}$ at 0.05, 0.1, 0.2, 0.3, 0.5, 0.7, 1.0, and 2.0 C, respectively. When the current was reversed to 0.1 C, the recovered specific discharge capacity corresponding to the P–$CoSe_2$@NGC/rGO−CNT-coated separator (958 mA h $g^{-1}$) was higher than that of the other coated separator interlayers, indicating the high reversibility of the redox processes. Furthermore, the capacity utilization values were calculated at different C rates for various coated separator arrangements, as summarized in Fig. 5l. The capacity utilization values, which measure the amount of active material consumed during the redox reaction, were the highest for the P–$CoSe_2$@NGC/rGO−CNT-coated separator cells. The high active material participation is consistent with the CV results, which demonstrate the lowest voltage hysteresis and superior electrocatalytic conversion capability of the P–$CoSe_2$@NGC/rGO−CNT microspheres.

The cycling performances of the assembled cells were further evaluated at low (0.1 and 0.5 C) and high (2.0 C) C rates. Fig. 6a and b depict

the cycling performance of the cells with different coating separator arrangements at 0.1 and 2.0 C, respectively. The cell with the P–$CoSe_2$@NGC/rGO−CNT-coated separator exhibited a higher initial discharge capacity of 1238 mA h $g^{-1}$ compared to P–$CoSe_2$@NGC (1144 mA h $g^{-1}$), F–$CoSe_2$@NGC (715 mA h $g^{-1}$), and P–CoO@NGC (792 mA h $g^{-1}$) coated separators. After 150 cycles, the capacity values for the P–$CoSe_2$@NGC/rGO−CNT- and P–$CoSe_2$@NGC-coated separator cells became similar, which agrees well with the rate capability tests shown in Fig. 1j. In contrast, the F–$CoSe_2$@NGC and P–CoO@NGC-coated separators consistently exhibited lower capacities throughout the cycling. However, when cycling was performed at a slightly higher C-rate of 0.5 C (Fig. S11), a noticeable difference in performance was observed, which became more prominent at a high C-rate of 2.0 C (Fig. 6b). For instance, the P–$CoSe_2$@NGC/rGO−CNT-coated separator exhibited an initial capacity of 433 mA h $g^{-1}$ and maintained almost 50 % of the capacity (217 mA h $g^{-1}$) after 1000 cycles. Moreover, a high Coulombic efficiency of 99.2 % at the 1000th cycle suggests high reversibility of the redox processes. In contrast, the P–$CoSe_2$@NGC-coated separator cell retained only 35 % (101 mA h $g^{-1}$) of its initial capacity (288 mA h $g^{-1}$). Furthermore, the cells with F–$CoSe_2$@NGC and P–CoO@NGC-coated separators exhibited inferior cycling performance. The high-capacity retention values of the P–$CoSe_2$@NGC/rGO−CNT microspheres confirmed the efficient anchoring of LiPSs within the cathodic domain, thereby reducing active material loss during prolonged cycling. These results strongly support the nanostructural advantages of the P–$CoSe_2$@NGC/rGO−CNT microspheres, which facilitate the effective capture of polysulfide species and suppress active material loss. Additionally, the improved redox kinetics support the smooth diffusion of charged species during the electrochemical processes, along with the effective absorption of undesired volume fluctuations due to the highly conductive and porous frameworks.

Electrochemical impedance spectroscopy (EIS) was employed to gain a deeper understanding of the enhanced redox kinetics. The EIS plots were obtained in the charge state at different cycle numbers during cycling at 2.0 C-rate, as shown in Fig. 6c. Nyquist plots were fitted with an equivalent circuit to analyze the Li–S cells utilizing various coated separators (Fig. S12). Notably, the Li–S cells featuring P–$CoSe_2$@NGC/rGO−CNT, P–$CoSe_2$@NGC, and P–CoO@NGC-coated separator displayed similar electrolyte resistance values ($R_e$; 4–6 Ω), indicating a stable electrode–separator–electrolyte interface. In contrast, the Li–S cells featuring the F–$CoSe_2$@NGC interlayer displayed the highest $R_e$ value (~33 Ω), suggesting that the filled morphology restricts the efficient electrolyte percolation inside the microspheres with relatively slow redox processes. Furthermore, the cell featuring the P–$CoSe_2$@NGC/rGO−CNT-coated separator exhibited the lowest $R_{ct}$ (~31 Ω) compared to the 3D P–$CoSe_2$@NGC (~78 Ω), F–$CoSe_2$@NGC (~80 Ω), and P–CoO@NGC (~62 Ω) coated separators. This trend persisted even after cycling, with the P–$CoSe_2$@NGC/rGO−CNT-coated separator maintaining the lowest $R_{ct}$ values at the 50th and 200th cycles, mainly because of the superior diffusion of the charged species during

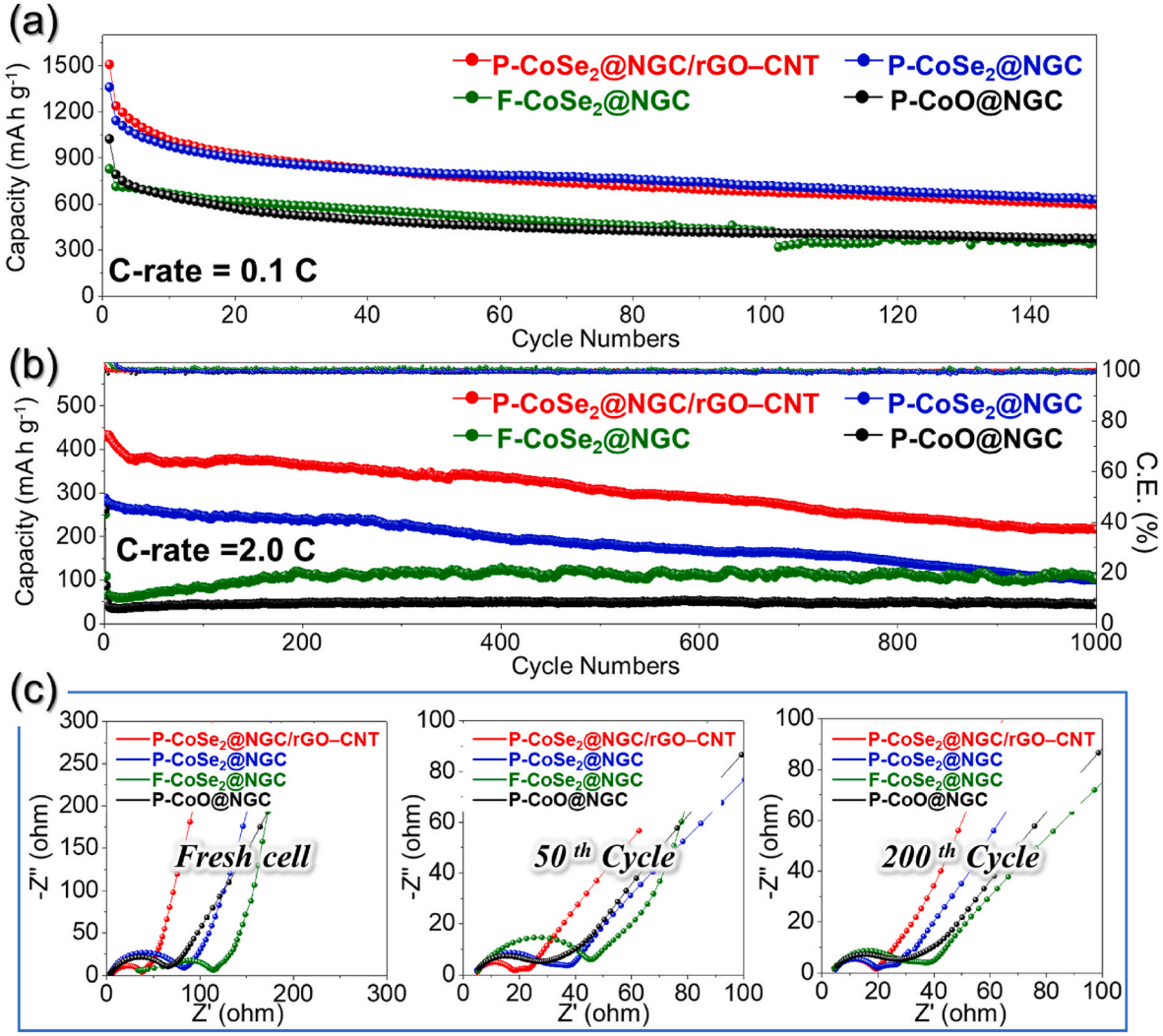


**Fig. 6.** Cycling performance of Li–S cells featuring different coated separators at (a) 0.1 C, (b) 2.0 C, and (c) Nyquist plots at different cycle numbers.

cycling. Specifically, at the end of the 200th cycle, the P–$CoSe_2$@NGC/rGO−CNT-coated separator exhibited an $R_{ct}$ of ~15 Ω, while P–$CoSe_2$@NGC, F–$CoSe_2$@NGC, and P–CoO@NGC-coated separators showed $R_{ct}$ values of approximately 27 Ω, 34 Ω, and 62 Ω, respectively. Additionally, the fading of two well-distinguished semicircles for P–$CoSe_2$@NGC/rGO−CNT-coated separator from 50th to 200th cycle indicates efficient catalytic conversion of nonconducting deposits of $Li_2S_2$ or $Li_2S$ during prolonged cycling [75]. This observation matches well with the cycling performance in Fig. 6b. Therefore, the lowest $R_{ct}$ values for P–$CoSe_2$@NGC/rGO−CNT-coated separator indicate improved redox kinetics, facilitating faster electrocatalytic conversion of polysulfides during the electrochemical processes. The electrochemical performance of the Li–S cell with a pristine separator is shown in Fig. S13, along with the corresponding discussion.

The P–$CoSe_2$@NGC/rGO−CNT-coated separator, serving as a multifunctional cathodic interlayer, underwent additional evaluation with more practical cell parameters: higher effective S-content (69 and 71 %), higher active material loading (3.5 and 4.6 mg $cm^{-2}$), and a leaner E/S ratio (7.4 and 5.6 μL $mg^{-1}$). The electrochemical results are shown in Fig. 7. The Li–S cell with a high-loading S electrode (3.5 mg $cm^{-2}$) exhibited notable rate capability performance (Fig. 7a). At C-rates of 0.1, 0.15, 0.2, 0.25, and 0.3 C, the cell achieved an initial discharge capacity of 982, 805, 679, 575, and 515 mA h $g^{-1}$, respectively. When the current was reversed, the cell regained its initial capacity after 0.1 C. The GCD voltage profiles in Fig. 7b confirm the presence of typical voltage plateaus associated with two-step sulfur redox reactions. The

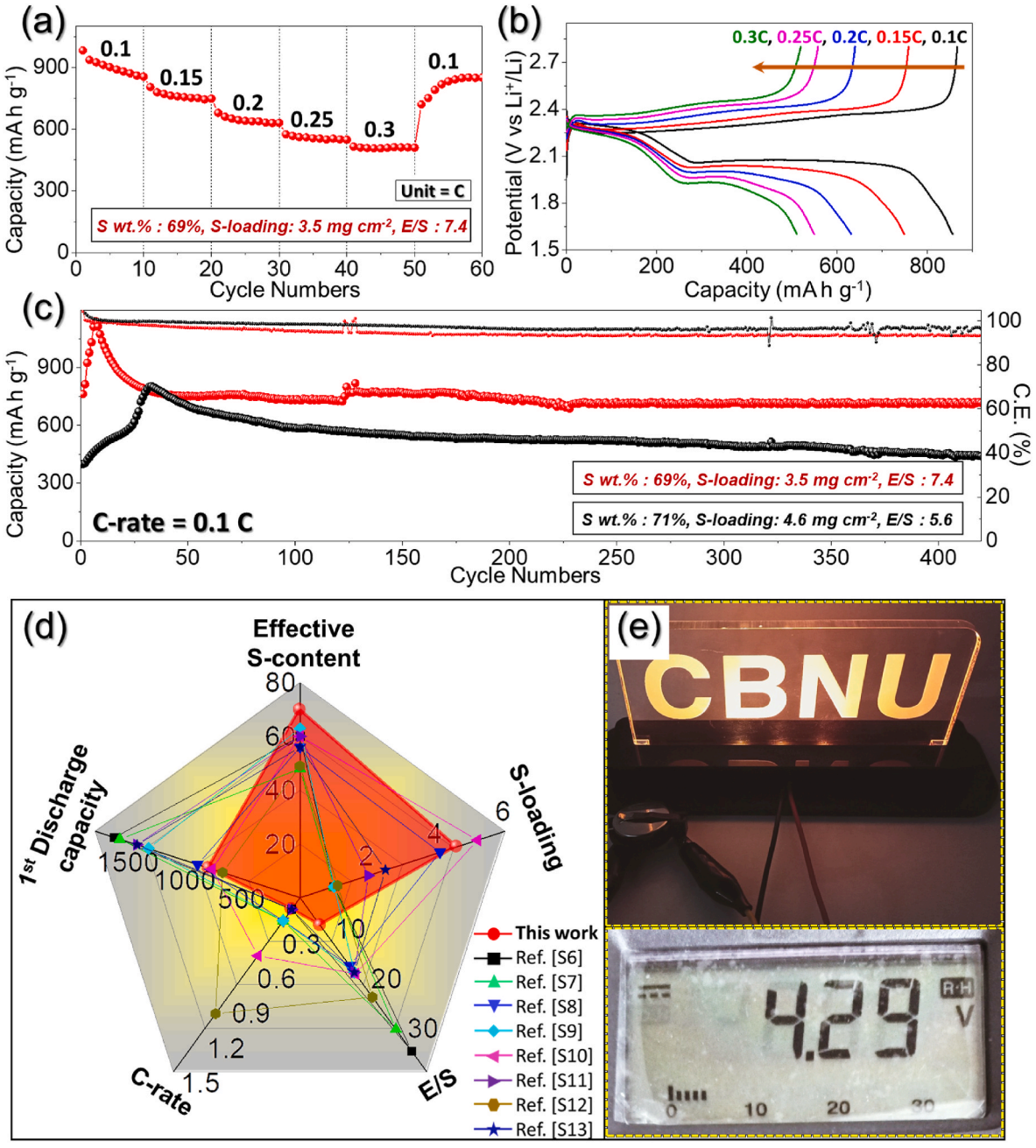


**Fig. 7.** (a) Rate capability results of Li–S featuring high-loading electrodes and P–$CoSe_2$@NGC/rGO−CNT-coated separator, (b) respective GCD voltage profiles of 10th cycle at various C-rates ranging from 0.1 to 0.3 C, (c) cycling performance with different cell parameters at 0.1 C, (d) comparison of the electrochemical performance obtained in this work to the previous reports, and (e) digital image of a light-emitting diode (5 V, 10 mW) powered by two cells utilized after cycling-performance tests at 0.1 C.

cycling performance at 0.1 C was further examined for the cells, as shown in Fig. 7c. With an active material loading of 3.5 mg $cm^{-2}$ and an E/S value of 7.4 μL $mg^{-1}$, the cell displayed an initial discharge capacity of 763 mA h $g^{-1}$, gradually increasing to 1009 mA h $g^{-1}$ in the initial cycles due to the activation process commonly observed with high-loading electrodes [22]. After 420 continuous cycles, the cell maintained a discharge capacity of 716 mA h $g^{-1}$ (94 % retention) with an average capacity decay rate of 0.01 %. Similar trends were observed when the sulfur loading and E/S values were adjusted to 4.6 mg $cm^{-2}$ and 5.7 μL $mg^{-1}$, respectively. The cell exhibited a discharge capacity of 439 mA h $g^{-1}$ after 420 continuous cycles. These electrochemical results, obtained with more feasible cell parameters, demonstrate the exceptional stability of the sulfur redox processes, which is primarily attributed to the robust nanostructures of the P–$CoSe_2$@NGC/rGO−CNT

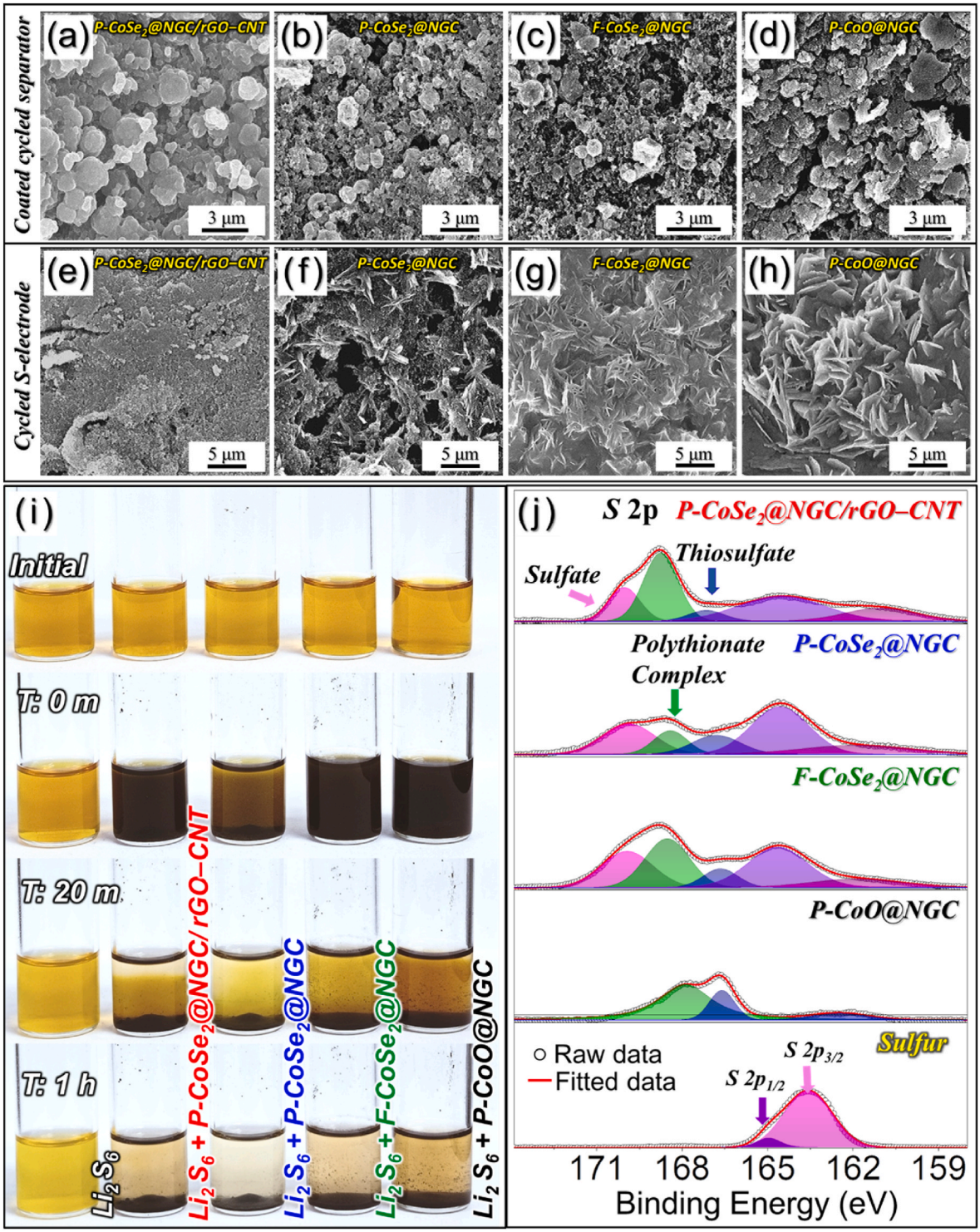


**Fig. 8.** Post-cycling characterization of the Li–S cells utilizing various coated separators: (a) FE-SEM micrograph of the P–$CoSe_2$@NGC/rGO−CNT, (b) P–$CoSe_2$@NGC, (c) F–$CoSe_2$@NGC, and (d) P–CoO@NGC-coated separators after cycling at 2.0 C, (e) FE-SEM micrograph of the cycled S-electrode paired with P–$CoSe_2$@NGC/rGO−CNT, (f) P–$CoSe_2$@NGC, (g) F–$CoSe_2$@NGC, and (h) P–CoO@NGC-coated separators, (i) Digital images of the polysulfide adsorption tests at different interval, and (j) S 2*p* XPS spectra of the powders collected from the cycled coated separators.

microspheres. Furthermore, the energy density of the cell utilizing high S-loading electrode was also calculated. Notably, the quasi-equilibrium reduction potential was calculated initially using the GITT analysis and used further to evaluate the energy density at electrode level. As observed from GITT profile in Fig. S14a, the quasi-equilibrium reduction potential is approximately 2.14 V (marked by black line). The cell with an active material loading of 3.5 mg $cm^{-2}$ resulted in a stable gravimetric energy density (electrode level) value of 1534 Wh $kg^{-1}$ at the end of 420th cycle, which is 59 % of the theoretical energy density (2600 Wh $kg^{-1}$). Fig. 7d and Table S2 summarize the electrochemical performances obtained in previous studies based on various practical parameters and compare them with the results of the present work. As shown in Fig. 7d, the cell performance is either superior or comparable to previous reports, thus demonstrating that the structural advantages of the P–$CoSe_2$@NGC/rGO−CNT microspheres not only guarantee efficient immobilization of the active material in the cathodic region but also ensure efficient electrocatalytic conversion. These observations highlight the potential of the proposed rational engineering strategy for the practical application of Li–S batteries, even under challenging battery conditions. To validate these findings, the cycled cells (Fig. 7c) were used to power a light-emitting diode (10 mW, 5 V), as illustrated in Fig. 7e. The series cell combination delivered uninterrupted power to the load for 0.5 h, confirming its suitability for practical applications.

### 3.4. Post-cycling characterizations of the cycled Li–S cells

Finally, after cycling at 2.0 C, the cells were disassembled to analyze the changes in the S electrode and coated separators. The FE-SEM micrograph in Fig. 8a reveals that the spherical morphology of the cycled P–$CoSe_2$@NGC/rGO−CNT-coated separator remained intact even after prolonged cycling (1000 cycles), primarily due to the self-supporting rGO−CNT framework that maintained its structural robustness. Furthermore, no evidence of polysulfide agglomeration was found on the spherical surface, indicating the effective electrocatalytic conversion of the trapped LiPS species. This observation is consistent with the FE-SEM image of the cycled sulfur electrode (Fig. 8e) paired with the P–$CoSe_2$@NGC/rGO−CNT-coated separator, which shows no sedimentation of foreign species. In contrast, the FE-SEM micrograph of the P–$CoSe_2$@NGC (Fig. 8b) suggests polysulfide agglomeration on the surface of the microspheres, accompanied by a slightly ruptured morphology owing to lower structural integrity or robustness. Similarly, the FE-SEM micrographs of the cycled F–$CoSe_2$@NGC and P–CoO@NGC-coated separators (Fig. 8c and d, respectively) indicate significant deposits of LiPSs and a complete destruction of the morphology. Additionally, the FE-SEM images of the cycled sulfur electrode paired with the P–$CoSe_2$@NGC, F–$CoSe_2$@NGC, and P–CoO@NGC-coated separators (Fig. 8f, g, and 8h, respectively) show extensive polysulfide accumulation, suggesting that the structures were not stable enough to withstand prolonged cycling. These post-cycling results further validate the idea that the structural integrity of the P–$CoSe_2$@NGC/rGO−CNT microspheres enable high utilization of the active material and minimizes parasitic polysulfide migration towards the Li anode. The visual demonstration of polysulfide adsorption tests (Fig. 8i) also confirmed these findings, as the color of the polysulfide solution changed from pale yellow to nearly clear (after T = 1 h) for the P–$CoSe_2$@NGC/rGO−CNT sample, indicating effective trapping of the polysulfide species by the polar $CoSe_2$ nanocrystals. The XPS spectra of the powders collected from the cycled coated separator were analyzed for the S 2*p* photoelectron signal (Fig. 8j), and a comparison was made with the S 2*p* spectrum of elemental sulfur. The S 2*p* signal for the cycled P–$CoSe_2$@NGC/rGO−CNT sample exhibited three distinct well-fitted peaks at 167.1, 168.7, and 170.0 eV corresponding to the thiosulfate ($-S_2O_3^{2-}$) and polythionate complexes and sulfate ($-SO_4^{2-}$) groups, respectively [30]. The presence of a thiosulfate peak indicates an interaction between the polysulfide species and $CoSe_2$ nanocrystals, facilitating the efficient anchoring of higher-order soluble LiPSs and their electrocatalytic conversion to lower-order insoluble polysulfides. The appearance of a peak corresponding to the polythionate complexes suggests a reaction between elemental sulfur and nucleophilic species, such as $HS^-$ or $SO_3^{2-}$, which is believed to suppress polysulfide crossover. The peak attributed to the sulfate ($-SO_4^{2-}$) species is a result of the decomposition of the LiTFSI salt during the redox processes and is considered a prime source of the $Li_xSO_y$ species. In contrast, the intensity of the polythionate complex peak was low for the cycled P–$CoSe_2$@NGC, F–$CoSe_2$@NGC, and P–CoO@NGC samples, indicating poor electrocatalytic conversion over extended cycling. These results further confirm the excellent capability of the 3D P–$CoSe_2$@NGC/rGO−CNT microspheres to suppress polysulfide diffusion, reduce active material loss, and enhance the electrochemical performance.

## 4. Conclusions

In summary, we employed a rationally engineered three-dimensional nanostructure composed of P–$CoSe_2$@NGC/rGO−CNT microspheres as a multifunctional cathodic interlayer to enhance the overall performance of Li–S batteries. These microspheres, synthesized via spray pyrolysis, consist of a highly conductive rGO−CNT framework for efficient charge transfer *via* primary and secondary pathways, the PS nanobead-derived macropores that facilitate the smooth diffusion of charged species by reducing the effective diffusion length, and the well-embedded $CoSe_2$ nanocrystals that serve as active chemisorption sites for the efficient trapping and electrocatalytic conversion of polysulfide species. The interlayer acts as “polysulfide sieves” to efficiently suppress the polysulfide crossover and improve the kinetics of sulfur redox reactions. Correspondingly, the Li–S cells incorporating the regular sulfur electrode and P–$CoSe_2$@NGC/rGO−CNT-coated separator demonstrate excellent rate capability (up to 2.0 C) and remarkable cycling stability with 1000 cycles at 2.0 C. Even under more demanding cell conditions, such as high sulfur content (71 %), high sulfur loading (4.6 mg $cm^{-2}$), and a low E/S (5.6 μL $mg^{-1}$) ratio, the cell exhibits impressive cycling stability with 420 cycles at 0.1 C, along with feasible rate performance up to 0.3 C. Overall, the structural and electrochemical advancements demonstrated in this study will provide valuable insights for the synthesis of structurally stable nanostructures, particularly in the context of metal sulfur battery applications.

## CRediT authorship contribution statement

**Rakesh Saroha:** Designed the study, performed experiments, and prepared the initial blueprint. **Hye Seon Ka:** Performed the experiments and collected the data. **Gi Dae Park:** Investigated the data. **Chungyeon Cho:** Collected the data. **Dong-Won Kang:** Writing – review & editing. **Jung Sang Cho:** Supervision, Writing – review & editing.

## Declaration of competing interest

The authors declare that they have no competing financial interests or personal relationships that may have influenced the work reported in this study.

## Data availability

No data was used for the research described in the article.

## Acknowledgments

This work was supported by the National Research Foundation of Korea (NRF) and funded by the Korean Government (MSIP) [grant numbers NRF-2021R1A4A2001687 and No. RS-2023-00217581]. This research was supported by "Regional Innovation Strategy (RIS)" through the National Research Foundation of Korea (NRF) funded by the Ministry of Education (MOE) (2021RIS-001) .

## Appendix A. Supplementary data

Supplementary data to this article can be found online at https://doi.org/10.1016/j.jpowsour.2023.233893.

## References


[1] X. Lu, X. Zhou, Q. Yang, X. Huang, Q. Zheng, D. Lin, Y. Song, J. Colloid Interface Sci. 600 (2021) 278–287, https://doi.org/10.1002/smll.202002213.
[2] R. Saroha, A.K. Panwar, Y. Sharma, P.K. Tyagi, S. Ghosh, Appl. Surf. Sci. 394 (2017) 25–36, https://doi.org/10.1016/j.apsusc.2016.09.105.
[3] R. Saroha, J.S. Cho, J.-H. Ahn, Electrochim. Acta 366 (2021), 137471, https://doi.org/10.1016/j.electacta.2020.137471.
[4] R. Saroha, A.K. Panwar, A. Jain, J. Singh, S. Verma, Ionics 23 (2017) 2631–2639, https://doi.org/10.1007/s11581-017-1984-2.
[5] J.H. Kim, B.R. Kim, J.S. Im, Kor. J. Chem. Eng. 40 (2023) 2839–2846, https://doi.org/10.1007/s11814-023-1529-5.
[6] S. Jayasubramaniyan, H.-W. Lee, Kor. J. Chem. Eng. 40 (2023) 488–496, https://doi.org/10.1007/s11814-022-1321-y.
[7] H. Wang, N. Deng, S. Wang, X. Wang, Y. Li, Q. Zeng, S. Luo, X. Cui, B. Cheng, W. Kang, J. Mater. Chem. A 10 (2022) 23433–23466, https://doi.org/10.1039/D2TA05576G.
[8] R. Saroha, A. Gupta, A.K. Panwar, J. Alloys Compd. 696 (2017) 580–589, https://doi.org/10.1016/j.jallcom.2016.11.199.
[9] Y. Gong, Y. Wang, Z. Fang, S. Zhao, Y.-s. He, W. Zhang, J. Mu, L. Zhang, Z.-F. Ma, Chem. Eng. J. 446 (2022), 136943, https://doi.org/10.1016/j.cej.2022.136943.
[10] R. Saroha, A.K. Panwar, Y. Sharma, Ceram. Int. 43 (2017) 5734–5742, https://doi.org/10.1016/j.ceramint.2017.01.115.
[11] R. Saroha, A.K. Panwar, A.R. Farooq, L. Krishniya, P. Tyagi, Ionics 23 (2017) 2641–2650, https://doi.org/10.1007/s11581-017-2000-6.
[12] Z. Li, Y. Huang, L. Yuan, Z. Hao, Y. Huang, Carbon 92 (2015) 41–63, https://doi.org/10.1016/j.carbon.2015.03.008.
[13] R. Saroha, J.-H. Ahn, J.S. Cho, Kor. J. Chem. Eng. 38 (2021) 461–474, https://doi.org/10.1007/s11814-020-0729-5.
[14] Z. Wu, L. Yuan, Q. Han, Y. Lan, Y. Zhou, X. Jiang, X. Ouyang, J. Zhu, X. Wang, Y. Fu, J. Power Sources 450 (2020), 227658, https://doi.org/10.1016/j.jpowsour.2019.227658.
[15] D. Son, W.-G. Lim, J. Lee, Kor. J. Chem. Eng. 40 (2023) 473–487, https://doi.org/10.1007/s11814-022-1372-0.
[16] Z. Zhang, Q. Li, S. Jiang, K. Zhang, Y. Lai, J. Li, Chem. Eur J. 21 (2015) 1343–1349, https://doi.org/10.1002/chem.201404686.
[17] W. Li, J. Hicks-Garner, J. Wang, J. Liu, A.F. Gross, E. Sherman, J. Graetz, J.J. Vajo, P. Liu, Chem. Mater. 26 (2014) 3403–3410, https://doi.org/10.1021/cm500575q.
[18] R. Saroha, J.H. Oh, Y.H. Seon, Y.C. Kang, J.S. Lee, J.S. Cho, J. Mater. Chem. A 9 (2021) 11651–11664, https://doi.org/10.1039/D1TA01802G.
[19] M. Tian, F. Pei, M. Yao, Z. Fu, L. Lin, G. Wu, G. Xu, H. Kitagawa, X. Fang, Energy Storage Mater. 21 (2019) 14–21, https://doi.org/10.1016/j.ensm.2018.12.016.
[20] R. Saroha, J.H. Oh, J.S. Lee, Y.C. Kang, S.M. Jeong, D.-W. Kang, C. Cho, J.S. Cho, Chem. Eng. J. 426 (2021), 130805, https://doi.org/10.1016/j.cej.2021.130805.
[21] S. Li, J. Warzywoda, S. Wang, G. Ren, Z. Fan, Carbon 124 (2017) 212–218, https://doi.org/10.1016/j.carbon.2017.08.062.
[22] R. Saroha, J.S. Cho, Small Methods 6 (2022), 2200049, https://doi.org/10.1002/smtd.202200049.
[23] M. Sevilla, J. Carro-Rodríguez, N. Díez, A.B. Fuertes, Sci. Rep. 10 (2020) 4866, https://doi.org/10.1038/s41598-020-61583-1.
[24] Y.H. Seon, R. Saroha, J.S. Cho, Compos. B Eng. 237 (2022), 109856, https://doi.org/10.1016/j.compositesb.2022.109856.
[25] Y. Hao, X. Li, X. Sun, C. Wang, ChemistrySelect 2 (2017) 9425–9432, https://doi.org/10.1002/slct.201701951.
[26] R. Saroha, Y.H. Seon, B. Jin, Y.C. Kang, D.-W. Kang, S.M. Jeong, J.S. Cho, Chem. Eng. J. 446 (2022), 137141, https://doi.org/10.1016/j.cej.2022.137141.
[27] M. Jana, R. Xu, X.-B. Cheng, J.S. Yeon, J.M. Park, J.-Q. Huang, Q. Zhang, H.S. Park, Energy Environ. Sci. 13 (2020) 1049–1075, https://doi.org/10.1039/C9EE02049G.
[28] R. Saroha, H.S. Ka, J.S. Cho, Appl. Surf. Sci. 612 (2023), 155892, https://doi.org/10.1016/j.apsusc.2022.155892.
[29] B. Li, Y. Pan, B. Luo, J. Zao, Y. Xiao, S. Lei, B. Cheng, Electrochim. Acta 344 (2020), 135811, https://doi.org/10.1016/j.electacta.2020.135811.
[30] J.M. Choi, R. Saroha, J.S. Kim, M.R. Jang, J.S. Cho, J. Power Sources 559 (2023), 232632, https://doi.org/10.1016/j.jpowsour.2023.232632.
[31] S. Yao, S. Xue, S. Peng, M. Jing, X. Shen, T. Li, Z. YiLiu, Int. J. Energy Res. 43 (2019) 1892–1902, https://doi.org/10.1002/er.4389.
[32] S.H. Yang, J.M. Choi, R. Saroha, S.W. Cho, Y.C. Kang, J.S. Cho, J. Colloid Interface Sci. 645 (2023) 33–44, https://doi.org/10.1016/j.jcis.2023.04.083.
[33] H. Yuan, X. Chen, G. Zhou, W. Zhang, J. Luo, H. Huang, Y. Gan, C. Liang, Y. Xia, J. Zhang, ACS Energy Lett. 2 (2017) 1711–1719, https://doi.org/10.1021/acsenergylett.7b00465.
[34] R. Saroha, J. Heo, X. Li, N. Angulakshmi, Y. Lee, H.-J. Ahn, J.-H. Ahn, J.-H. Kim, J. Alloys Compd. 893 (2022), 162272, https://doi.org/10.1016/j.jallcom.2021.162272.
[35] J. Li, C. Jiao, J. Zhu, L. Zhong, T. Kang, S. Aslam, J. Wang, S. Zhao, Y. Qiu, J. Energy Chem. 57 (2021) 469–476, https://doi.org/10.1016/j.jechem.2020.03.024.
[36] R. Saroha, J. Heo, Y. Liu, N. Angulakshmi, Y. Lee, K.-K. Cho, H.-J. Ahn, J.-H. Ahn, Chem. Eng. J. 431 (2022), 134205, https://doi.org/10.1016/j.cej.2021.134205.
[37] Y.X. Yao, X.Q. Zhang, B.Q. Li, C. Yan, P.Y. Chen, J.Q. Huang, Q. Zhang, InfoMat 2 (2020) 379–388, https://doi.org/10.1002/inf2.12046.
[38] X.-B. Cheng, J.-Q. Huang, Q. Zhang, J. Electrochem. Soc. 165 (2017) A6058, https://doi.org/10.1149/2.0111801jes.
[39] H.-L. Wu, M. Shin, Y.-M. Liu, K.A. See, A.A. Gewirth, Nano Energy 32 (2017) 50–58, https://doi.org/10.1016/j.nanoen.2016.12.015.
[40] Y. Xiang, J. Li, J. Lei, D. Liu, Z. Xie, D. Qu, K. Li, T. Deng, H. Tang, ChemSusChem 9 (2016) 3023, https://doi.org/10.1002/cssc.201600943.
[41] Q. Wu, X. Zhou, J. Xu, F. Cao, C. Li, J. Energy Chem. 38 (2019) 94–113, https://doi.org/10.1016/j.jechem.2019.01.005.
[42] L. Fan, M. Li, X. Li, W. Xiao, Z. Chen, J. Lu, Joule 3 (2019) 361–386, https://doi.org/10.1016/j.joule.2019.01.003.
[43] Z. Jian, H. Li, R. Cao, H. Zhou, H. Xu, G. Zhao, Y. Xing, S. Zhang, Electrochim. Acta 319 (2019) 359–365, https://doi.org/10.1016/j.electacta.2019.06.145.
[44] J. He, A. Bhargav, H. Yaghoobnejad Asl, Y. Chen, A. Manthiram, Adv. Energy Mater. 10 (2020), 2001017, https://doi.org/10.1002/aenm.202001017.
[45] G.G. Kumar, S.-H. Chung, T. Raj Kumar, A. Manthiram, ACS Appl. Mater. Interfaces 10 (2018), 20627, https://doi.org/10.1021/acsami.8b06054.
[46] C. Lu, R. Fang, K. Wang, Z. Xiao, G.G. Kumar, Y. Gan, X. He, H. Huang, W. Zhang, Y. Xia, Front. Chem. 9 (2021), 738977, https://doi.org/10.3389/fchem.2021.738977.
[47] M. Li, D. Yang, J.J. Biendicho, X. Han, C. Zhang, K. Liu, J. Diao, J. Li, J. Wang, M. Heggen, Adv. Funct. Mater. 32 (2022), 2200529, https://doi.org/10.1002/adfm.202200529.
[48] S.H. Chung, A. Manthiram, Adv. Mater. 26 (2014) 1360–1365, https://doi.org/10.1002/adma.201304365.
[49] G.G. Kumar, M. Christy, H. Jang, K.S. Nahm, J. Power Sources 288 (2015) 451, https://doi.org/10.1016/j.jpowsour.2015.04.029.
[50] G. Siva, M.A. Aziz, G.G. Kumar, ACS Sustain. Chem. Eng. 6 (2018) 5929, https://doi.org/10.1021/acssuschemeng.7b04326.
[51] G. Ahmed, F.A. Butt, F. Raza, S. Hashmi, G.G. Kumar, M. Christy, J. Power Sources 538 (2022), 231379, https://doi.org/10.1016/j.jpowsour.2022.231379.
[52] M.Y. Oh, J.J. Lee, A. Zahoor, G.G. Kumar, K.S. Nahm, RSC Adv. 6 (2016), 32212, https://doi.org/10.1039/C6RA02459A.
[53] Y. Luo, H. Bai, B. Li, X. Song, J. Zhao, Y. Xiao, S. Lei, B. Cheng, J. Alloys Compd. 879 (2021), 160368, https://doi.org/10.1016/j.jallcom.2021.160368.
[54] J.S. Lee, M.S. Jo, R. Saroha, D.S. Jung, Y.H. Seon, J.S. Lee, Y.C. Kang, D.W. Kang, J. S. Cho, Small 16 (2020), 2002213, https://doi.org/10.1002/smll.202002213.
[55] D. Yin, J. Tang, R. Bai, S. Yin, M. Jiang, Z. Kan, H. Li, F. Wang, C. Li, Nanoscale Res. Lett. 16 (2021) 1–10, https://doi.org/10.1186/s11671-020-03469-9.
[56] C.S. Kim, J.S. Lee, R. Saroha, Y.B. Park, Y. Chan Kang, D.-W. Kang, S.M. Jeong, J. S. Cho, J. Power Sources 523 (2022), 231030, https://doi.org/10.1016/j.jpowsour.2022.231030.
[57] L. Li, Q. Yuan, S. Ye, Y. Fu, X. Ren, Q. Zhang, J. Liu, Mater. Chem. Front. 5 (2021) 6171–6181, https://doi.org/10.1039/D1QM00627D.
[58] J.S. Lee, R. Saroha, J.S. Cho, Nano-Micro Lett. 14 (2022) 1–22, https://doi.org/10.1007/s40820-022-00855-z.
[59] C.S. Kim, R. Saroha, H.H. Choi, J.H. Oh, G.D. Park, D.-W. Kang, J.S. Cho, J. Ind. Eng. Chem. 121 (2023) 489–498, https://doi.org/10.1016/j.jiec.2023.02.004.
[60] S.-K. Park, Y.C. Kang, ACS Appl. Mater. Interfaces 10 (2018) 17203–17213, https://doi.org/10.1021/acsami.8b03607.
[61] J.S. Lee, R. Saroha, J.H. Oh, C. Cho, B. Jin, D.-W. Kang, J.S. Cho, J. Ind. Eng. Chem. 114 (2022) 276–287, https://doi.org/10.1016/j.jiec.2022.07.017.
[62] S.H. Oh, S.M. Park, D.-W. Kang, Y.C. Kang, J.S. Cho, J. Ind. Eng. Chem. 83 (2020) 438–448, https://doi.org/10.1016/j.jiec.2019.12.017.
[63] R. Saroha, H.H. Choi, J.S. Cho, Chem. Eng. J. 473 (2023), 145391, https://doi.org/10.1016/j.cej.2023.145391.
[64] J.S. Lee, H.S. Ka, R. Saroha, Y.C. Kang, D.-W. Kang, J.S. Cho, J. Energy Storage 66 (2023), 107396, https://doi.org/10.1016/j.est.2023.107396.
[65] J.S. Lee, J.-S. Park, K.W. Baek, R. Saroha, S.H. Yang, Y.C. Kang, J.S. Cho, Chem. Eng. J. 456 (2023), 141118, https://doi.org/10.1016/j.cej.2022.141118.
[66] C.S. Kim, R. Saroha, J.S. Cho, Int. J. Energy Res. 2023 (2023), https://doi.org/10.1155/2023/3610577.
[67] J.S. Lee, R. Saroha, S.H. Oh, D.H. Shin, S.M. Jeong, J.K. Kim, J.S. Cho, Small Methods (2021), 2100195, https://doi.org/10.1002/smtd.202100195.
[68] R. Saroha, A.K. Panwar, J. Phys. D Appl. Phys. 50 (2017), 255501, https://doi.org/10.1088/1361-6463/aa708c.
[69] Z.-G. Pi, H. Ye, Z. Han, P. Yu, Z. Yin, X. Ma, Front. Mater. 9 (2022), 1005221, https://doi.org/10.3389/fmats.2022.1005221.
[70] Y. Tang, Z. Zhao, X. Hao, Y. Wang, Y. Liu, Y. Hou, Q. Yang, X. Wang, J. Qiu, J. Mater. Chem. A 5 (2017) 13591–13600, https://doi.org/10.1039/C7TA02665J.
[71] P. Rani, K.S. Kumar, A.D. Pathak, C.S. Sharma, Appl. Surf. Sci. 533 (2020), 147483, https://doi.org/10.1016/j.apsusc.2020.147483.
[72] B. Liu, V.S. Thoi, Chem. Commun. 58 (2022) 4005–4015, https://doi.org/10.1039/D1CC07087H.
[73] H. Zhou, Q. Tang, Q. Xu, Y. Zhang, C. Huang, Y. Xu, A. Hu, X. Chen, RSC Adv. 10 (2020) 18115–18123, https://doi.org/10.1039/D0RA02833A.
[74] J. Zhou, R. Li, X. Fan, Y. Chen, R. Han, W. Li, J. Zheng, B. Wang, X. Li, Energy Environ. Sci. 7 (2014) 2715–2724, https://doi.org/10.1039/C4EE01382D.
[75] Z.A. Ghazi, X. He, A.M. Khattak, N.A. Khan, B. Liang, A. Iqbal, J. Wang, H. Sin, L. Li, Z. Tang, Adv. Mater. 29 (2017), 1606817, https://doi.org/10.1002/adma.201606817.